2014-09

Implementation of an optical readout system for high-sensitivity terahertz microelectromechanical sensor array

Toh, Edwin

Monterey, California: Naval Postgraduate School

NAVAL POSTGRADUATE SCHOOL

MONTEREY, CALIFORNIA

THESIS

IMPLEMENTATION OF AN OPTICAL READOUT SYSTEM FOR HIGH-SENSITIVITY TERAHERTZ MICROELECTROMECHANICAL SENSOR ARRAY

by

Edwin Toh

September 2014

Thesis Advisor: Gamani Karunasiri
Co-Advisor: Fabio Alves

THIS PAGE INTENTIONALLY LEFT BLANK

REPORT DOCUMENTATION PAGE

Form Approved OMB No. 0704–0188

1. AGENCY USE ONLY *(Leave blank)*	**2. REPORT DATE** September 2014	**3. REPORT TYPE AND DATES COVERED** Master's Thesis

4. TITLE AND SUBTITLE
IMPLEMENTATION OF AN OPTICAL READOUT SYSTEM FOR HIGH-SENSITIVITY TERAHERTZ MICROELECTROMECHANICAL SENSOR ARRAY

5. FUNDING NUMBERS

6. AUTHOR(S) Edwin Toh

7. PERFORMING ORGANIZATION NAME(S) AND ADDRESS(ES)
Naval Postgraduate School
Monterey, CA 93943-5000

8. PERFORMING ORGANIZATION REPORT NUMBER

9. SPONSORING /MONITORING AGENCY NAME(S) AND ADDRESS(ES)
N/A

10. SPONSORING/MONITORING AGENCY REPORT NUMBER

11. SUPPLEMENTARY NOTES The views expressed in this thesis are those of the author and do not reflect the official policy or position of the Department of Defense or the U.S. Government. IRB Protocol number ____N/A____.

12a. DISTRIBUTION / AVAILABILITY STATEMENT
Approved for public release; distribution is unlimited

12b. DISTRIBUTION CODE

13. ABSTRACT (maximum 200 words)

In this thesis, an optical readout scheme was successfully developed based on the Fourier 4F optical configuration and integrated with a custom-fabricated microelectromechanical system (MEMS)-based, terahertz (THz), detector array. The MEMS THz detector array and 4F Fourier optics were able to transduce the THz scene into an optical signal that was captured by a commercial charged coupled device (CCD) camera for generating images. A quantum cascade laser (QCL) provided the THz illumination for generating images while post-image processing performed background subtraction in order to obtain the THz scene. The Fourier 4F optical readout system that was implemented was able to profile the general shape of the QCL beam pattern and displayed good linearity of response of about 23 gray level values per Kelvin. The concept of optical readout from a micromechanical sensor array was also validated.

14. SUBJECT TERMS terahertz imager, Terahertz MEMS, optical readout	**15. NUMBER OF PAGES** 73
	16. PRICE CODE

17. SECURITY CLASSIFICATION OF REPORT	**18. SECURITY CLASSIFICATION OF THIS PAGE**	**19. SECURITY CLASSIFICATION OF ABSTRACT**	**20. LIMITATION OF ABSTRACT**
Unclassified	Unclassified	Unclassified	UU

NSN 7540–01-280-5500

Standard Form 298 (Rev. 2–89)
Prescribed by ANSI Std. 239–18

THIS PAGE INTENTIONALLY LEFT BLANK

Approved for public release; distribution is unlimited

IMPLEMENTATION OF AN OPTICAL READOUT SYSTEM FOR HIGH-SENSITIVITY TERAHERTZ MICROELECTROMECHANICAL SENSOR ARRAY

Edwin Toh
Captain, Republic of Singapore Army
B.Eng., National University of Singapore, 2009

Submitted in partial fulfillment of the
requirements for the degree of

MASTER OF SCIENCE IN COMBAT SYSTEMS TECHNOLOGY

from the

NAVAL POSTGRADUATE SCHOOL
September 2014

Author: Edwin Toh

Approved by: Gamani Karunasiri
Thesis Advisor

Fabio Alves
Co-Advisor

Andres Larraza
Chair, Department of Physics

THIS PAGE INTENTIONALLY LEFT BLANK

ABSTRACT

In this thesis, an optical readout scheme was successfully developed based on the Fourier 4F optical configuration and integrated with a custom-fabricated microelectromechanical system (MEMS)-based, terahertz (THz), detector array. The MEMS THz detector array and 4F Fourier optics were able to transduce the THz scene into an optical signal that was captured by a commercial charged coupled device (CCD) camera for generating images. A quantum cascade laser (QCL) provided the THz illumination for generating images while post-image processing performed background subtraction in order to obtain the THz scene. The Fourier 4F optical readout system that was implemented was able to profile the general shape of the QCL beam pattern and displayed good linearity of response of about 23 gray level values per Kelvin. The concept of optical readout from a micromechanical sensor array was also validated.

THIS PAGE INTENTIONALLY LEFT BLANK

TABLE OF CONTENTS

THIS PAGE INTENTIONALLY LEFT BLANK

LIST OF FIGURES

THIS PAGE INTENTIONALLY LEFT BLANK

LIST OF TABLES

THIS PAGE INTENTIONALLY LEFT BLANK

LIST OF ACRONYMS AND ABBREVIATIONS

CCD	charged coupled device
CMOS	complementary metal oxide semiconductor
COTS	commercial off the shelf
FPA	focal plane array
II	image intensifiers
IR	infrared radiation
MEMS	microelectromechanical systems
NEP	noise equivalent power
QCL	quantum cascade laser
RTD	resonant tunnel diodes
SNR	signal-to-noise ratio
THz	terahertz

THIS PAGE INTENTIONALLY LEFT BLANK

ACKNOWLEDGMENTS

Without the help and support of the following people, my thesis would not have been possible.

Professor Gamani Karunasiri allowed me the opportunity to contribute toward the efforts of the sensor research team. I am also thankful for his guidance and confidence. His support and advice helped me greatly during the preparation of this thesis.

I would also like to acknowledge Dr. Fabio Alves for sharing his invaluable knowledge with me, as well as spending hours in the laboratory helping me with the experimental setup and design. His sharing of experiences and practical insights made my efforts for this thesis much simpler.

Finally, I would like to acknowledge my wife, Jasmin, who supported me greatly throughout my coursework at NPS.

THIS PAGE INTENTIONALLY LEFT BLANK

I. INTRODUCTION

The terahertz (THz) spectral range, especially within the 0.3 to 10 THz frequencies, has continued to generate interest for imaging and spectrometry applications. THz wavelengths, which are in the sub-millimeter range, are small enough to be able to provide good resolution in imaging and yet also long enough to be able to penetrate thin, non-metallic, and non-polarizing dielectric materials like clothing and plastic packaging [1]. In addition, numerous explosives and chemical and biological weapons have unique THz spectra responses that can be used for detection and identification [2], [3]. More importantly, THz radiation is also non-ionizing and potentially safe [4], making it attractive for applications seeking human exposure. As a result, there has been increasing interest in THz generation and detection.

To this end, the Sensors Research Lab (SRL) at the Naval Postgraduate School has commenced research work in THz sensing and THz imaging. Early research work focused on utilizing a quantum cascade laser (QCL) as a THz source and uncooled microbolometer cameras as detectors [5], [6]. Subsequently, the research evolved to focus on highly absorbing thin films and metamaterial structures. This effort culminated in the design and fabrication of novel microelectromechanical systems (MEMS) bi-material THz focal plane array (FPA) by Alves et al. [7]–[10]. This FPA consists of an array of THz absorbing elements, each attached to bi-material Al/SiO_x cantilever legs. These legs are anchored to a Si substrate. The absorbing element absorbs the incident THz radiation and the heat causes deformation of the bi-material legs. The amount of deformation of the legs has been probed by an optical readout system. Similar optical readout techniques have also been widely used for IR detection [11]–[13].

Based on the custom fabricated FPA, Montagner [14] proposed an optical readout design to be integrated with a THz imagining system. The design leverages external THz illumination and allows for the displacement of all the sensors in the focal plane array (FPA) to be simultaneously measured and to generate an image using a charged couple device (CCD) camera.

A. OBJECTIVE

Moving forward, building upon all the work done previously, the aim of this thesis is to develop an optical readout scheme utilizing the MEMS based THz sensor to perform imaging under THz illumination.

Specifically, this thesis involves integration of a THz QCL as an illumination source, the MEMs sensor, and optical readout system in order to produce an active, real-time, and standoff THz imaging system operating in transmission mode.

The proposed setup would specifically consist of a milliwatt scale QCL providing active, external illumination onto the MEMS THz FPA. The FPA, which is enclosed in a vacuum chamber, would also be illuminated by an external light source and the optical system would project the reflected light from the FPA onto a CCD camera. The image information from the CCD is then fed onto custom image processing software, designed using LabVIEW, to perform image background subtraction for sensor displacement visualization and real-time image generation.

Characterization of the THz imaging system will be done and readout analysis will be performed as part of this thesis.

B. ORGANIZATION OF THESIS

This thesis is organized as follows.

- Chapter I provides the background as well as the main objective of this thesis.
- Chapter II provides an overview of different approaches employed in THz imaging.
- Chapter III highlights the main motivations behind the development of the MEMS-based THz sensor and the main features of the integrated THz imaging system. The various components of the system are also introduced.
- Chapter IV explains the concept of operations of the main components and how they contribute to the overall functionality of the integrated system.

- Chapter V provides the imaging results and their analysis.
- Chapter VI presents the conclusion of this thesis research and suggestions for possible future work.

THIS PAGE INTENTIONALLY LEFT BLANK

II. OVERVIEW OF THZ IMAGING SYSTEMS

Over the past decade, THz imaging systems have been developed to provide better performance, simpler operation, and greater portability. This overview provides a general survey of THz sources, THz detectors and sensors, as well as imaging systems to provide an understanding of the important aspects of THz imaging.

A. THZ SOURCES

THz radiation is part of the continuous electromagnetic wave spectrum. Hence, THz can be emitted by blackbodies, as described by Planck's radiation law. THz frequencies between 1 to 10 THz are the characteristic peak frequencies of blackbody radiation curves of temperatures between 10 to 100 K. Naturally occurring THz sources of importance include dust clouds from distant galaxies as well as the cosmic microwave background radiation, which is now cooled to below the lower frequency end of the THz spectrum. As such, natural THz radiation has important implications in astrophysics [15].

For practical imaging applications, THz radiation is usually generated to illuminate the object. Some generation techniques include the use of negative differential devices, stimulated emission from lasers, acceleration and deceleration of electric charges, as well as frequency manipulation by converting other electromagnetic frequencies to the THz range.

The nonlinear current-voltage characteristics of solid-state electronic devices can be used to generate THz radiation [16]. THz radiation is generated in this manner by Gunn diodes, IMPATT diodes, and resonant tunneling diodes (RTD).

THz radiation can also be generated by stimulated emission within a gain medium enclosed in a cavity. The generation technique is similar to that developed for lasers whereby THz emission takes place when an electron transits from a high-energy to low-energy state. The key to successful emission is the maintenance of the population inversion in the gain medium by a pump. THz lasers have been generated at low temperatures by a Si gain medium doped with P and Bi, and optically pumped by a free electron laser [17]. For high-powered applications, optically pumped THz lasers are

usually preferred due to their simplicity and high signal-to-noise ratio (SNR). The average power for such lasers has been reported to be around 100 mW [18].

Accelerating electric charges using magnetic fields can also generate THz radiation. Gyrotrons have been shown to produce very powerful coherent and high-powered THz beams with peak power between 0.3 to 1.8 kW in 8 μs pulses with a frequency range of 0.55 to 1 THz [19].

In addition, devices such as frequency multipliers and photomixers can also generate THz radiation. Frequency multipliers make use on non-linear devices to convert a laser beam into two lower frequency beams. An example of such a non-linear device is an optical parametric oscillator such as $LiNbO_3$, which has been reported to generate THz radiation with cryogenic cooling [20]. In the case of photomixers, a pair of optical or infrared lasers is irradiated onto a photoconductive semiconductor antenna, usually made of GaAs. The laser energies are greater than the band gap of the semiconductor and this induces a photocurrent with different frequency. By properly selecting the frequencies of the lasers, THz radiation can be generated. The key characteristics of this generation technique is that THz radiation can be generated as a continuous wave or as pulses with a very long coherence length of up to 8 m at a frequency of approximately 1 THz [21].

Quantum cascade lasers (QCLs) are semiconductor-based lasers that can also emit THz radiation. Unlike traditional semiconductor lasers whereby photons are emitted when electrons from the conduction band recombine with holes in the valance band, QCLs exploit electron transitions between sub-energy states within the conduction band. This is because quantum confinement splits the conduction band energy levels into sub-energy levels. This quantum confinement effect is mainly due to the fabrication of alternate layers of different semiconductor materials (e.g., AlGaAs and GaAs) with different band gap energy. Most QCLs operate based on a three-level energy system. Transitions occur sequentially from level 3 to level 1, and the cascading effect is apparent when an electron is able to produce many photons as it transits through the levels. The limitations of QCL include the need to be cryogenically cooled and a limited frequency-tuning range [22]. While QCLs have limited frequency bandwidth, compared to other

broad bandwidth systems, QCLs can be tuned to achieve high power for deeper transmittance through objects.

B. THZ DETECTION SCHEMES

There are two main schemas in THz detection, incoherent or coherent detection. In incoherent detection, otherwise known as direct detection, the incident radiation is directly converted to heat or used to create charge carriers (i.e., the output from the detector is directly proportional to the incident power of the radiation). Examples of direct detectors include Schottky diodes, bolometers, thermopiles, pyroelectrics, and Golay cells.

On the other hand, coherent detection involves mixing the incident radiation frequency to the frequency from a local oscillator to obtain a lower value, intermediate frequency. The intermediate frequency is the difference between the incident frequency and the frequency of the local oscillator. Subsequently, the intermediate frequency is amplified. Coherent detection not only detects the power of the incident radiation but also the phase [23].

The incoherent detection scheme is a much simpler approach as compared to the coherent detection scheme as it only detects the intensity changes while coherent detection captures both the intensity and phase information of the radiation.

C. CLASSIFICATION AND TYPES OF THZ DETECTORS

THz detectors can be broadly classified as thermal detectors or photon detectors [15]. Thermal detectors generally absorb the incident THz radiation, which causes change in some physical property, which can be probed by a readout circuit. Bolometers and pyroelectric detectors and Golay cells belong to this category.

Bolometers are basically made up of materials that change their electrical resistance with temperature as they are exposed to radiation. Microbolometers, which can be considered as a class of bolometers, are uncooled arrays of bolometers that have similar operating principles to those of bolometers. They measure the amount of THz radiation by measuring the change in electrical resistance due to temperature change as

radiation is absorbed. The most common bolometric materials are made of amorphous silicon or vanadium oxides. They generally have a noise equivalent power (NEP) of approximately 300 pW in the THz range [24] and 14 pW in the IR range [8]. Hence, these microbolometers are generally optimized for IR detection rather than for THz detection. A key limitation for microbolometers is that detector FPA has to be integrated with a readout circuit, which is used to measure the thermoelectric resistance of the detector. This generally makes the fabrication more complex and adds noise to the detection.

Pyroelectric detectors exploit the fact that pyroelectric crystals vary their electric polarization as the temperature changes. The pyroelectric crystals are then implemented as capacitors with two electrodes mounted perpendicularly to the direction of spontaneous polarization. When incident THz radiation is absorbed, there will be a temperature change which results in polarization and change in the charge within the crystal capacitor. It has been reported that pyroelectric crystals have a responsivity of 1 kV/W and NEP of approximately 10^9 W/Hz$^{1/2}$ [25].

Golay cells consist of a sealed container, containing a gas with low thermal conductivity within a flexible window with reflective material. The window is illuminated with an external light source and photo detectors track the displacements of the flexible window. When THz radiation is absorbed, it heats the gas in the Golay cell and causes the gas volume to increase, displacing the window proportionally. The reflected light from the window is displaced and the intensity of the incident THz radiation can be inferred. For imaging applications, it has been reported that Golay cell micro arrays based on a graphene membrane have been developed with a responsivity of 400 nm/K [26].

Another class of thermal THz detectors is the MEMS bi-material sensor that makes use of meta-material absorbers. This class of detector has been developed by our group and will be described in Chapter III.

The detectors mentioned previously are classified as thermal detectors. The second class of THz detectors is photon detectors. Photon detectors produce an electric

current when incident THz radiation is absorbed [27]. This occurs when the incident THz radiation interacts with the electrons in the lattice atoms, electrons from the dopant atoms or free electrons. The incident THz radiation is able to excite these electrons across the band gap to induce a photocurrent [15], which is probed by a readout circuit.

An example of a photon detector is the Schottky barrier diode, which can also be used to detect THz radiation. An output voltage is produced in the Schottky barrier diode that is proportional to the power of the input current when it is being induced by THz radiation [28]. It has a non-linear current-voltage relationship, which means it can be used in a heterodyne receiver for coherent scheme detection. In other applications, it has been reported being able to provide wide bandwidth and high sensitivity by coupling it to an antenna and a parabolic mirror to collect the THz radiation [29].

D. THZ IMAGING

THz imaging systems can be broadly classified as active or passive imaging systems. Active imaging systems illuminate the target with an external THz source and the scattered THz radiation is detected. On the other hand, passive imaging relies on emitted or scattered THz radiation by a target with no external THz source illumination. Both imaging systems can operate in either reflection or transmission mode. Generally, passive imaging systems rely on room temperature illumination for indoor applications and sky illumination for outdoor applications.

As a comparison of passive and active imaging systems, images from passive systems are more influenced by the object's thermal emissivity and temperature. Images from active systems are more influenced by the angle between the source of illumination and returns received by the detector from the target's surface [30]. Passive imaging systems are more susceptible to thermal noise while active imaging systems require high-power THz sources to be effective.

THIS PAGE INTENTIONALLY LEFT BLANK

III. IMAGING SYSTEM SETUP

This chapter introduces the various sub-system components in the proposed imaging system setup. The considerations and limitations of each component will also be briefly highlighted to derive the rationale for the design of the experimental setup. The general features of the system will also be introduced to explain the key concepts of operation of the entire system.

A. MOTIVATIONS BEHIND THE DEVELOPMENT OF THE MEMS THZ OPTICAL READOUT SYSTEM

An alternative to the various detection methods and schemes described in Chapter II are MEMS cantilever detectors utilizing optical or capacitive readout schemes. The cantilever based MEMS detectors have been successfully developed for infrared (IR) detection and imaging [31]. In the optical readout system developed for this thesis, the MEMS detector consists of an array of sensing elements (THz absorbers), which absorb incoming THz radiation and convert it into heat. The heat is then transmitted by conduction to bi-material legs, which undergo bi-metallic deformation when there are temperature changes. This bi-metallic deformation is then probed by an optical readout by reflecting light off it, as each sensor element has an embedded reflective Al surface as the ground plate. When operated in this manner, each sensing element in the MEMS detector acts as a pixel for the optical readout.

The motivation behind the development of the MEMS THz optical readout system is as follows.

- MEMS-based sensors with optical readout schemes are able to leverage commercial-off-the-shelf (COTS) charged coupled devices (CCD), image intensifiers (II), or complementary metal oxide semiconductor (CMOS) cameras to be used as THz imagers. This can potentially drive down the cost of THz imagers and encourage greater adoption.

- Optical readout schemes allow the MEMS sensor device to be physically isolated from the readout system, which is not possible for current bolometer based THz imagers. This isolation provides extra design freedom and simpler construction, as well as potentially minimizes the thermal noise.

- Unlike bolometers (which are based on changes in electrical resistance with temperature) whereby the responsivity is dependent on the temperature sensitive material used in the sensor, the MEMS bi-material sensors can be designed with the same materials with different responsivity based on the geometrical parameters.

B. DESIGN OF THE SYSTEM

The schematics of the overall system and the picture of the actual imaging system setup are shown in Figure 1 and Figure 2, respectively. The entire system consists of four main parts:

- The QCL
- The THz MEMS bi-material FPA
- Fourier 4F optical readout system
- Image processing utility software developed using LABview

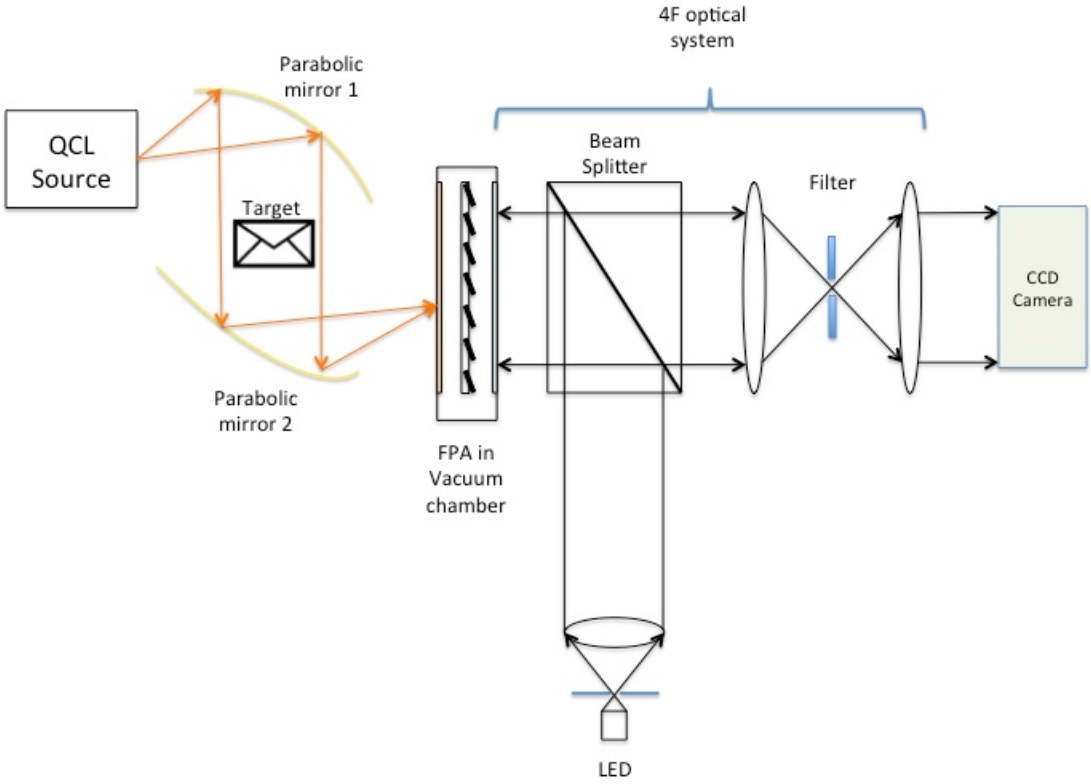

Figure 1. Schematic diagram showing the optical readout system. All major components are shown here. The transmitted THz beam is absorbed by the MEMS detector, which causes thermo-mechanical deflection of the bi-material sensor. This deflection is probed by the Fourier 4F optical system and fed to the CCD camera for imaging.

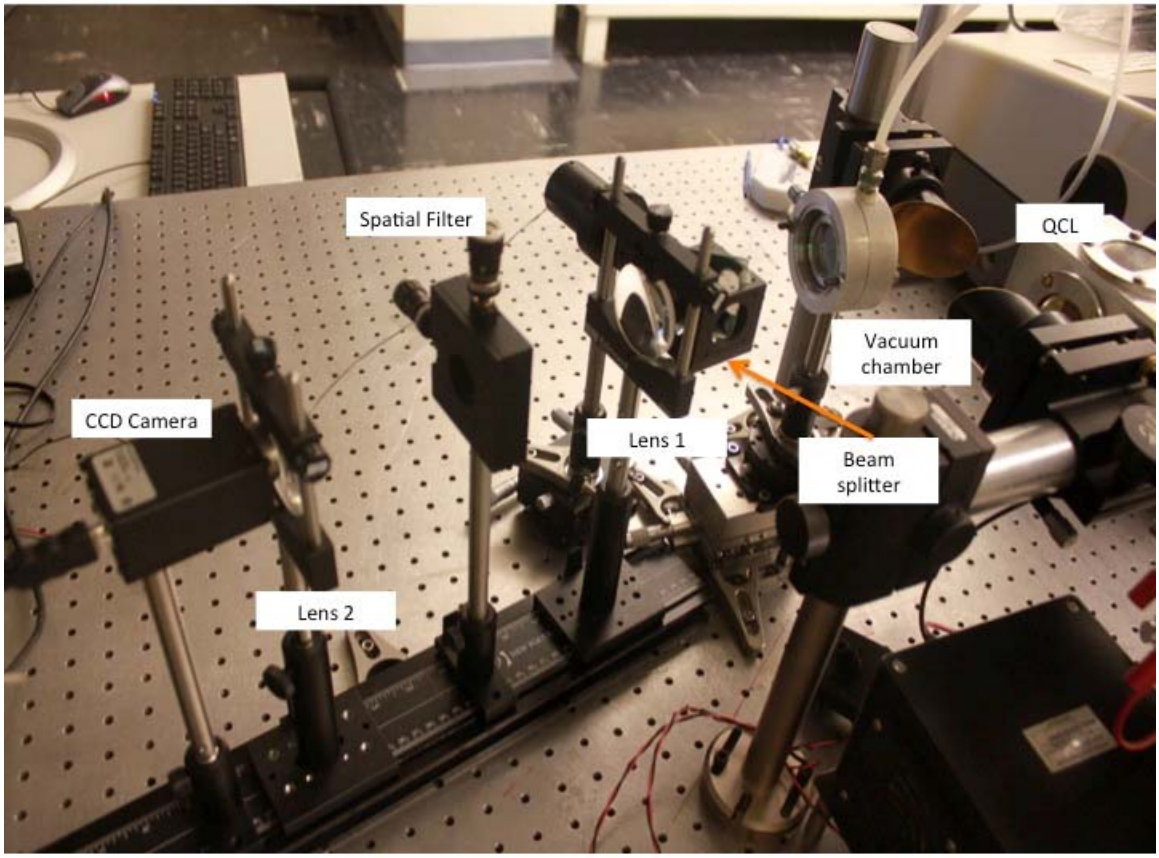

Figure 2. Actual imaging system setup, which was implemented in the laboratory. The Fourier 4F optical readout assembly is offset to compensate for the intrinsic tilting of the absorbers due to residual stress during fabrication.

C. GENERAL FEATURES OF THE SYSTEM

The following general system features provide real-time and high-frame rate imaging capabilities.

1. Optical Readout from Sensor

Optical readout from the sensor enables it to maintain high sensitivity with very low crosstalk. Optical readout schemes are also relatively simple to design as compared to complex, integrated microelectronic readout schemes. In this setup, the images obtained from the readout are fed to image-processing software for downstream processing and image enhancements.

2. Multiple Pixel Probing

The MEMS sensor is physically isolated from the optical readout system and the displacement of each pixel is optically tracked. The optical readout system is able to process the displacement of each pixel simultaneously. Hence, multiple pixels could be probed at the same time in order to generate the THz scene.

3. Differential Imaging

Due to the use of bi-materials, the sensors in the MEMS detector have residual stress and this causes the legs and the absorber of the sensor to have an intrinsic deflection. As the sensors absorb THz radiation, the bi-material legs increase in temperature causing further deflections. Differential imaging was used to eliminate the intrinsic bending pattern and detect changes from the initial resting position of the sensor.

For the setup, the differential imaging involves capturing the background information initially and storing it in memory. This background image is then subtracted from subsequent images captured in order to produce a difference between the two. This difference reveals the displacement information of each sensor on the THz FPA. In turn, the displacement information directly relates to the amount of THz radiation, which is absorbed by the sensors at each location. This concept of operation is further elaborated in the later part of this chapter.

D. COMPONENTS OF THE SYSTEM

The individual components used in system are highlighted in the following sections.

1. The Sensor

The sensor used in the system is the heart of the THz imaging system. The MEMS biomaterial FPA used in this work was designed and fabricated by Alves et al. [32]. It is a thermo-mechanical sensor, which converts THz energy absorbed into mechanical displacement. The performance parameters of the sensor are strongly influenced by the

materials used in the detector and the geometry of the design. These performance parameters are shown in Table 1.

Table 1. Measured performance parameters of MEMS detector. From [32].

Absorbance, η	Time constant, τ (s)	Responsivity, dθ/dP ($\times 10^6$ Deg W^{-1})	Thermo-mechanical sensitivity, dT/dP (Deg K^{-1})	Noise Equivalent Power, NEP ($\times 10^{-9}$ W)
0.95	0.8	1.2	0.2	8.6

The MEMS detector used consists of an array of THz absorbers. Each absorber element also has 10 × 10 square meta-material sensing elements, which were optimized to absorb at 3.8 THz of the QCL. In addition, each absorber is connected to the Si substrate by rectangular bi-material legs to a supporting anchor made of SiOx. The bi-material legs and the anchor conduct heat away from the absorber to the Si substrate. The Si substrate acts as a heat sink for this purpose. Incident THz radiation is converted into heat by the absorbers. This heat is then transmitted through the bi-material legs. The transmitted heat causes the temperature of the legs to increase and undergo bi-metallic deformation. This, in turn, alters the angular deflection of the absorber, which is then probed by an optical readout by reflecting light by the Al ground plane. The structure of a sensor in the FPA is illustrated in Figure 3.

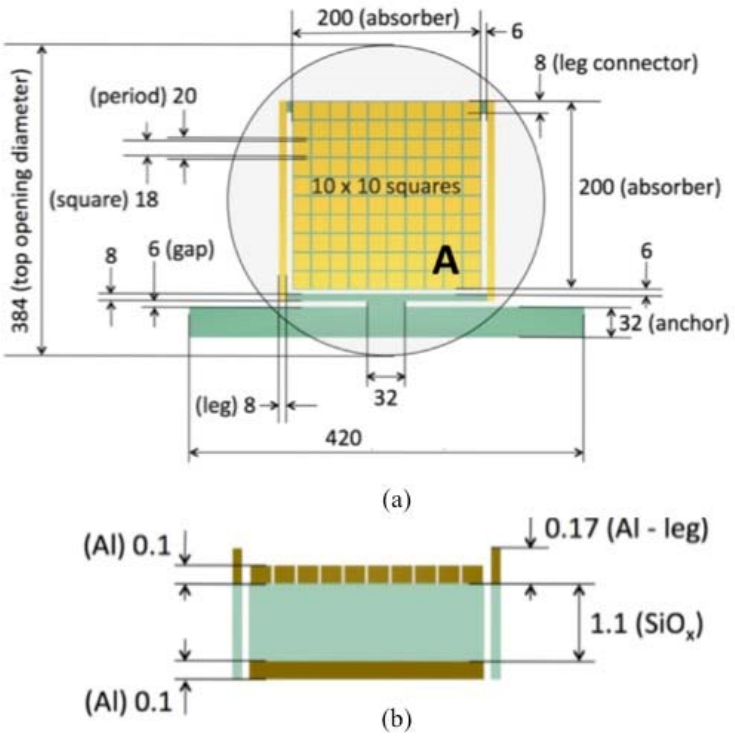

Figure 3. MEMS bi-material THz sensor pixel used for the system (all dimensions are in μm). (a) Top view of each sensor. (b) Vertical cross section of the absorber and bi-material legs. Square meta-material structure on top of the absorber provides strong THz absorbance while the Al ground plate provides the reflective surface for optical readout. From [32].

The performance parameters highlighted in Table 1 are independent from the optical readout except the NEP. It establishes the intrinsic limits of the sensor, which are dependent on the structure of the sensor and the materials used. The intrinsic noise of the sensor includes temperature fluctuation noise, background fluctuation noise, and thermo-mechanical noise [33]. Temperature fluctuation noise is a result of conductive heat exchange of between the sensor and the surroundings due to the temperature fluctuations between them. As a result, the sensor tip constantly fluctuates. Thermo-mechanical noise is an inherent property of the sensor caused by the exchange of mechanical energy between the sensor and the external environment. In this case, the mechanical structure acts as a resonator, which can store and dissipate mechanical energy. The oscillations of the cantilever structure are directly proportional to the thermal energy of the cantilever.

Background fluctuation noise is caused by the temporal fluctuations in the radiative heat absorbed by the sensor. The primary heat exchange mechanism in this case is radiation between the sensor and the background. Temperature fluctuation noise, thermo-mechanical noise, and background fluctuation noise contribute to the overall fluctuations in the sensor deflection. This differs from the readout noise, which is mainly due to illumination source fluctuation and mechanical vibrations in the readout system.

2. Sensor Vacuum Chamber

Temperature fluctuation noise, background fluctuation noise, and thermo-mechanical noise cannot be prevented. However, it is still possible to mitigate convective heat exchange between the sensor and the ambient surroundings. To mitigate the effects of convective heat exchange, the sensor is placed in a vacuum chamber at a pressure of approximately 4 x 10^{-5} mbar in order to minimize heat exchange between the sensor and the surrounding ambient environment. The vacuum chamber was custom fabricated at the Naval Postgraduate School and is shown in Figure 4.

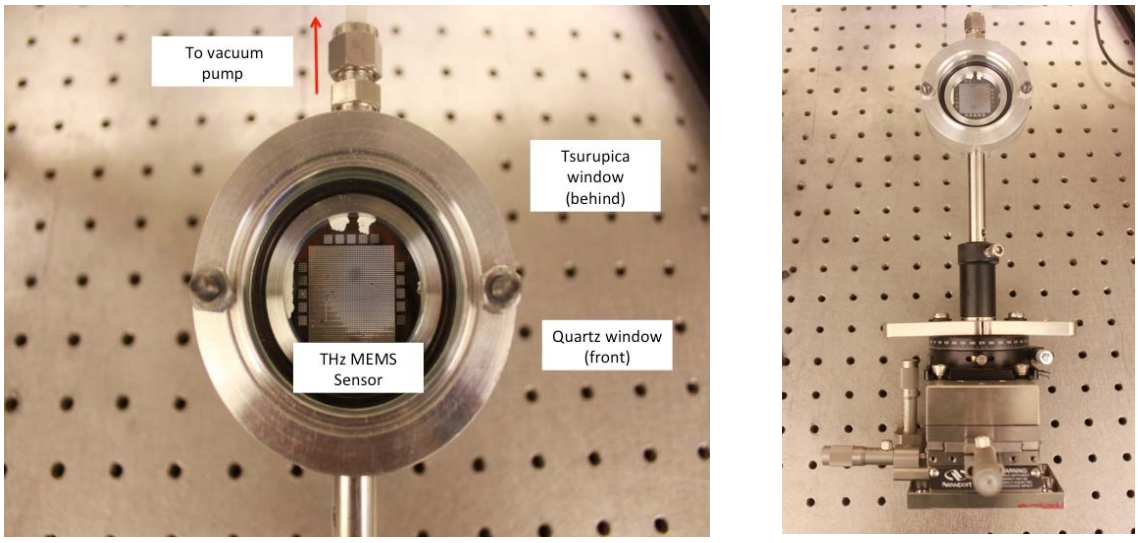

(a) (b)

Figure 4. Vacuum chamber used to house sensors to minimize convective heat exchange. (a) Closeup front view of vacuum chamber with mounted MEMS THz sensor array with the front and back transmission windows. (b) Vacuum chamber mounted on precision rotating stage for alignment purposes.

The vacuum chamber has a front tsurupica window and back quartz window. The front tsurupica window has approximately 80 percent transmittance at 3.8 THz [34] to allow most of the QCL THz radiation to reach the MEMS detector. The quartz window has an anti-reflective coating to allow maximum transmission of visible light from the readout side of the detector. Finally, the entire vacuum chamber is mounted on a 3-axis micrometer driven rotating stage to facilitate alignment as shown in Figure 4(b).

3. THz Source – Quantum Cascade Laser (QCL)

A THz-QCL is used as the illumination source since it provides the most suitable means to generate THz radiation. QCL-based THz sources are simpler and more compact than other sources (see Figure 5) and can provide power at a milliwatt range.

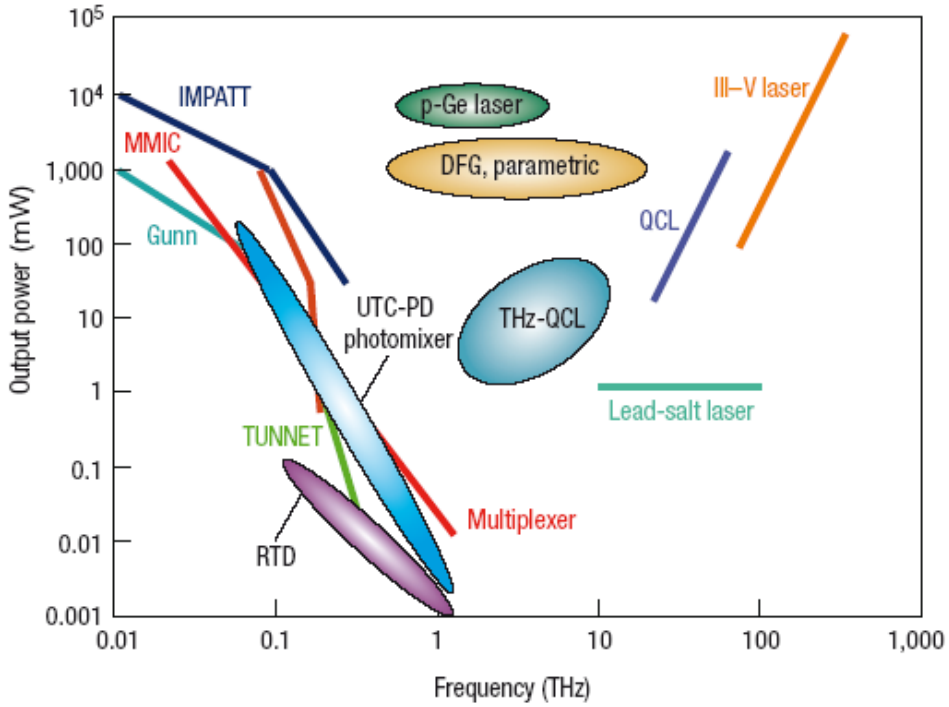

Figure 5. Plot of output power against THz frequency for the various methods to produce THz radiation. It can be seen that from the required output and frequency, THz-QCL provides the most suitable means. From [35].

A QCL of approximately 3.8 THz is used as an illuminating source during the measurements. The continuous electrical pumping of the QCL results in rapid joule

heating, which causes degradation of output power. Therefore, the QCL is operated in pulsed mode and cooled down to approximately 10 to 15 K for effective operation. Figure 6 shows the QCL and the cryostat assembly.

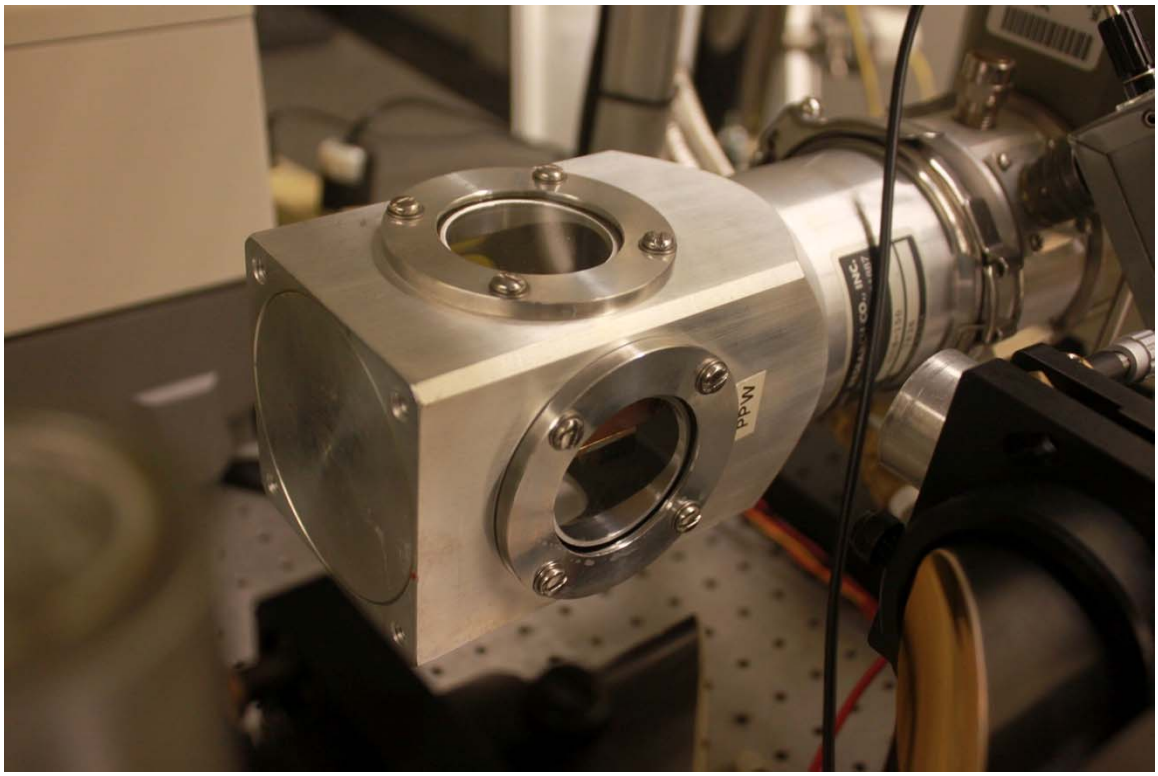

Figure 6. QCL and cryostat assembly. The QCL needs to be housed in the cryostat chamber to be cooled for effective power output. The QCL head is visible through the tsurupica window of the cryostat assembly. The tsurupica window is used to allow maximum transmission of the generated THz radiation from the QCL.

The QCL is driven by an AVTECH pulsed laser diode driver, AVO-6HZ-B. It is also gated with an Agilent Technologies 33522A function/arbitrary waveform generator. For normal operations, the QCL is operated at a pulse repetition frequency (PRF) between 0.5 to 10 kHz, at a constant pulse width of 5 μs and gated at 500 mHz to prevent the laser from overheating so that the laser performance does not degrade. However, for short durations of approximately 15 to 20 seconds, the gating can be switched off for generating greater power. The QCL performance parameters used are summarized in Table 2.

Table 2. QCL parameters used for THz imaging. The measured peak frequency and spectral width were obtained from [36].

Peak frequency (THz)	Full width half maximum spectral width of QCL (GHz)	Pulse repetition frequency (kHz)	Operating laser Pulse width (μs)	Output power (μW)	QCL gating frequency (mHz)
3.78	30	0.5-10	5	~1	500

4. THz Beam Focusing Optics

The QCL source generates THz radiation as a highly divergent beam in a concentric ring pattern as shown in Figure 7 (from [36]).

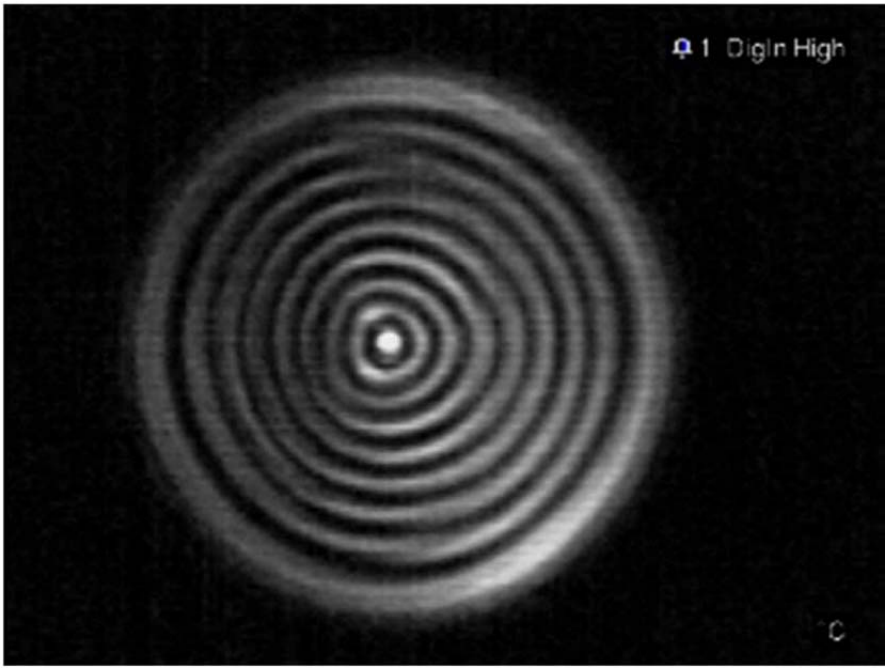

Figure 7. Imaging of QCL THz laser beam using a microbolometer camera. The beam was imaged using two converging lenses by Ng [36]. It can be observed that the THz beam pattern consists of concentric rings. These rings are caused by far field interference due to multiple facets of the QCL.

To focus the THz beam energy onto the sensor, it is necessary to use focusing optics. Off-axis parabolic (OAP) mirrors were selected because they are able to reflect light from a point source and convert it to a collimated beam off axis. The collimated region is to provide an area for the target to be imaged. The OAP mirrors used are gold plated for maximum reflectance.

For the setup, two OAP metal mirrors (f1 and f2) are used to focus and steer the beam. The f1 (focal length=50.8 mm) OAP is used to collimate the emerging THz beam while the f2 (focal length=101.8 mm) OAP is used to focus the beam onto the sensor. The OAP mirrors are configured to be as close as possible with each other to minimize the optical path so as to reduce beam losses due to absorption. The use of OAP mirrors is preferred over lenses to focus the THz beam because the OAP mirrors absorb less THz radiation as compared to tsurupica lenses. The downside is that OAP mirrors are much harder to align.

5. 4F Optical System

Figure 8 shows the optical readout system used for the THz imaging. It is composed of a collimated light source, a beam splitter, a pair of lenses (focal length=10 cm), and an aperture, which acts as a spatial filter.

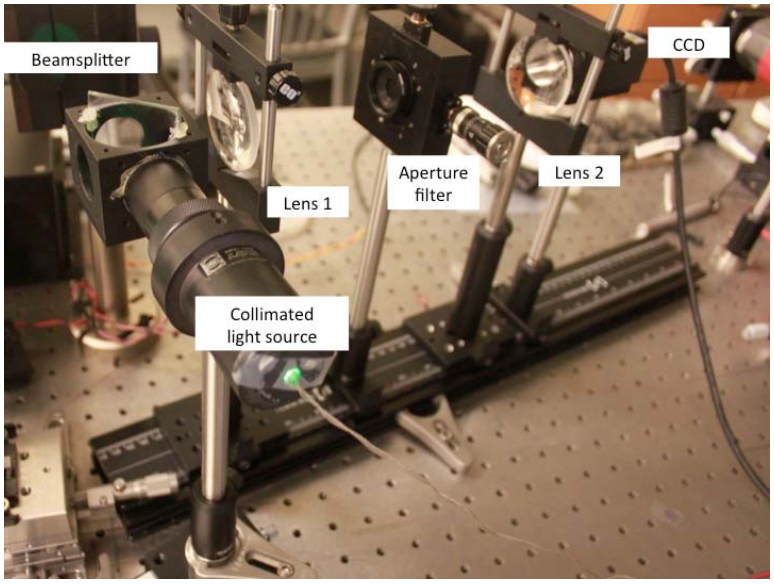

Figure 8. Optical readout system. The system is mounted on an optical rail for alignment purposes.

The 4F optical system is a "perfect imaging system," whereby all rays emerging from a single point in an object space would re-converge and form another point in the image space after passing through the system [37]. This allows the optical scene from the sensor (input plane) to be imaged onto the CCD camera sensor (output plane). Moreover, the Fourier plane between the lenses allows spatial filtering to be performed. Spatial filtering allows the system to have increased sensitivity for the optical readout.

For our application, an aperture is used in the Fourier plane to serve two purposes.

- The aperture would be able to block deflected rays from the sensor and thus provide spatial filtering for enhanced sensitivity. This concept of operation will be further elaborated in Chapter IV.

- The aperture acts as a low pass filter and applies a Gaussian blur to the image to reduce image noise [38]. This is a simple approach to reduce image noise without having to implement digital processing downstream in the system. In addition, it provides better control for the user to determine the amount of detail to be revealed during the imaging.

The main limitation of utilizing a 4F optical system was that it was relatively difficult to align it with the MEMS THz sensor.

6. Collimated Optical Light Source

The light source used for readout is a high-power light-emitting diode (LED), CREE 941-XPEGRNL 100A01, biased at a voltage of approximately 3 V and current 350 mA. This allows the LED to emit green light at a theoretical maximum of 87.4 lm [39]. The LED is placed behind a small aperture to act as a point source. The light emitted is collimated by a converging lens before it reaches the beamsplitter. The collimated LED assembly is shown in Figure 9.

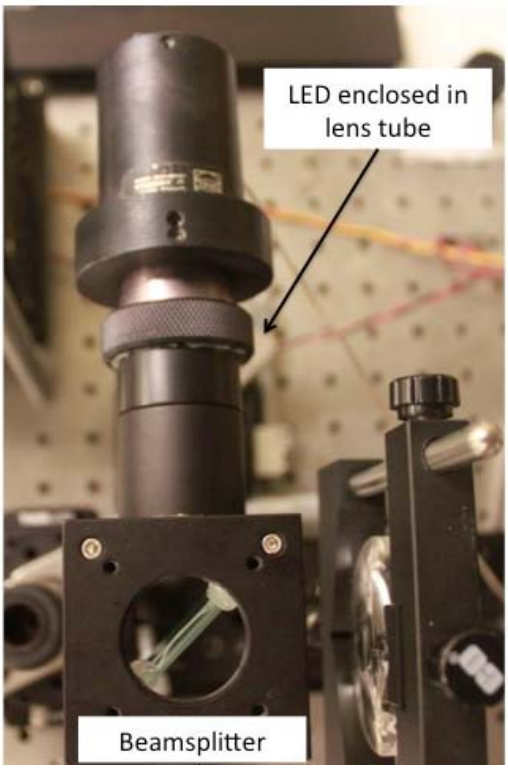

Figure 9. Top view of the self-aligned collimated LED assembly. The LED point source was enclosed in a lens tube produce a collimated output. The beam splitter reflects the collimated light onto the MEMS detector and the reflected light from the MEMS detector is then transmitted through the beamsplitter to the Fourier 4F optical system.

7. CCD Camera

The model of the CCD camera used is a Basler A631f. The purpose of the CCD camera is to convert the image into a digital format for post processing. The CCD camera has 1392 x 1040 pixels. Each pixel measures 4.65 x 4.65 μm, which is of sufficient resolution to image each pixel from the MEMS THz sensor FPA. The output of the camera has 8 bits per pixel, which allows a maximum of 255 gray values. These gray values allow the indirect measurement of the relative intensities of the reflected light on the CCD sensor. In addition, the camera has a maximum frame rate of 18.7 fps, which is fast enough for our imaging application. To complement the maximum sensitivity of the CCD camera, the green light source from the LED is used to illuminate the sensor.

8. Differential Imaging Software

The digital signal from the CCD camera is fed to custom-designed imaging software developed by Montagner [14]. The imaging software is programmed using LabVIEW, developed by National Instruments. The high-level flowchart describing differential imaging performed in LabVIEW is shown in Figure 10.

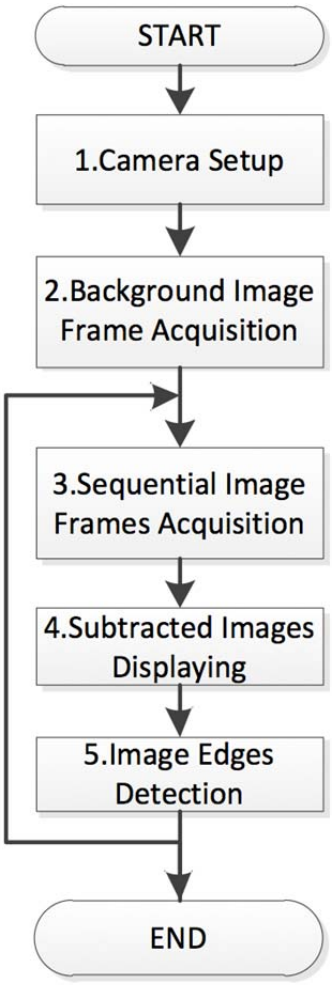

Figure 10. Steps used in differential imaging using LabVIEW. Step 1 requires the user to determine the gain and shutter settings of the camera. These settings affect the image quality. Step 2 obtains the background image without illumination and step 3 obtains the image with illumination. Step 4 does the most important function to form the THz image. Step 5 involves detecting local discontinuities in the pixel intensities by allowing the user to determine the range of pixel gray values that would be replaced by a specific one. From [14].

The imaging software works by capturing an initial frame as a background image. Subsequent images acquired by the camera are processed by subtracting from the background image. This is an indirect means to visualize the displacement of the sensors in the FPA, which is a result of the THz scene on the FPA. For the subtracted image display, there are two options available:

- Simple subtraction whereby the gray scale value recorded by each pixel in the CCD sensor is subtracted from the gray scale value from the same pixel in the background image acquisition. The result can either be a positive or negative value.

- Absolute subtraction whereby the gray scale value is the absolute value obtained from simple subtraction.

The developed software could also perform image edge detection in the final step. The image edge detection could identify edges by associating big changes in pixel intensity values as edges. For the setup, absolute subtraction is preferred as it is the simplest means to measure the absolute displacement of the sensor, which corresponds to the relative intensity of THz radiation received by the sensors. This is a suitable means to visualize the amount of THz radiation incident on the sensor, as the setup would mainly operate in transmission mode.

In addition, the imaging software allows a specific area on the obtained image to be surveyed. This allows the statistical measurement of pixel intensities of the obtained image for characterization purposes. The graphical user interface of the imaging software is shown in Figure 11, and a screenshot showing a specific area survey for statistical measurement is shown in Figure 12.

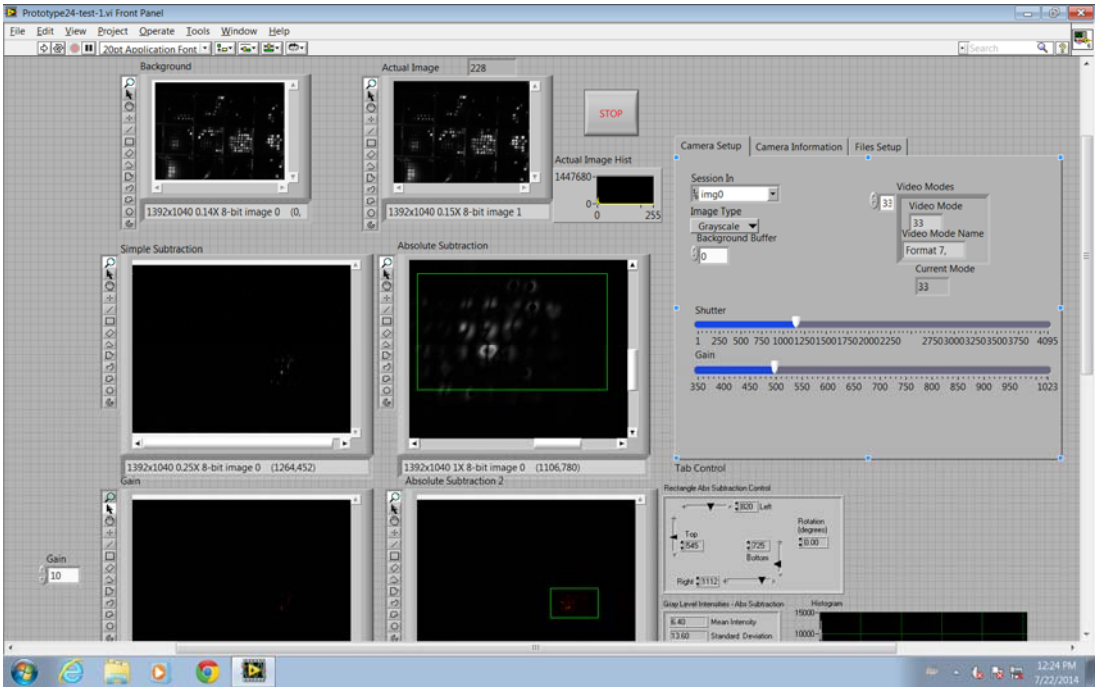

Figure 11. Graphical user interface of imaging software developed using LabVIEW. The results from the absolute subtraction due to sensor deflection are shown in the last screen on the second row. Various functions are available to allow the user to adjust the image quality obtained.

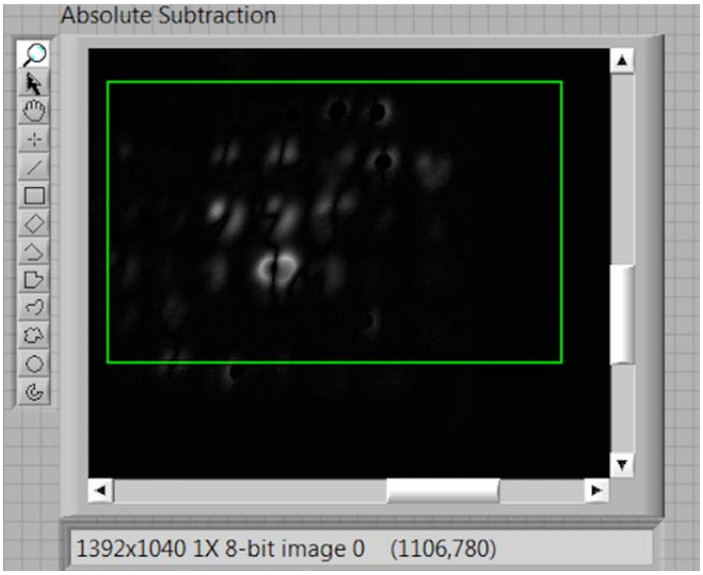

Figure 12. Screenshot showing a specific area (selected in the green box) for statistical measurement. The mean intensity and standard deviation of the gray values within the green box will be calculated by the program and provided to the user.

IV. IMPLEMENTATION AND CONCEPT OF OPERATION OF THE IMAGING SYSTEM

This chapter details the specific measures used to integrate the various components of the imaging system and the concept of operation for the imaging system.

A. FPA AND OPTICAL SYSTEM ALIGNMENT

The imaging system is implemented with an angular offset between the vacuum chamber housing the sensor and the 4F optical readout system due to intrinsic bending (due to residual stress) of the bi-material pixels. The intrinsic bending is measured and found to be approximately 8^{o} with respect to the substrate plane [32]. This is shown in Figure 13.

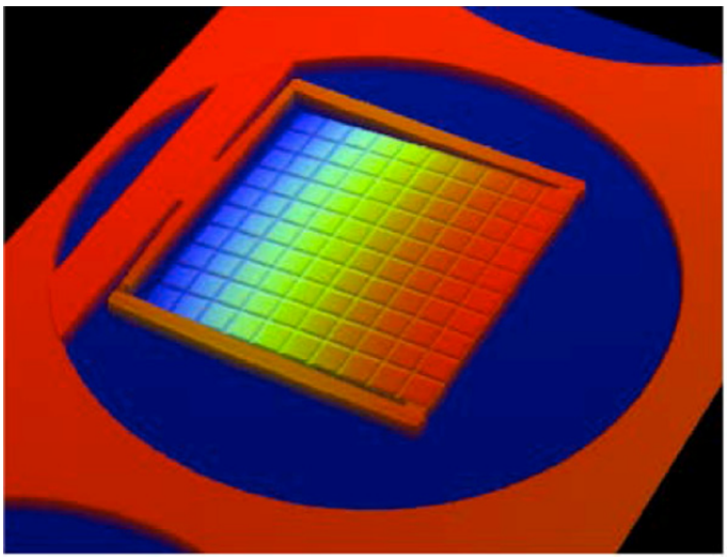

Figure 13. 3D profile plot of sensor showing the intrinsic bending of the sensor. From [9].

The sensor FPA is positioned perpendicular to the incident THz radiation and the optical readout system is offset at an angle. This differs from another approach adopted by Grbovic [33] to compensate for the intrinsic deformation of an IR sensor during fabrication. In that approach, the angular position of the FPA was adjusted instead. This difference is illustrated in Figure 14. Grbovic's approach is illustrated in Figure 14(a)

while the approach adopted for this thesis is illustrated in Figure 14(b). The offset in the actual setup can be seen in Figure 15.

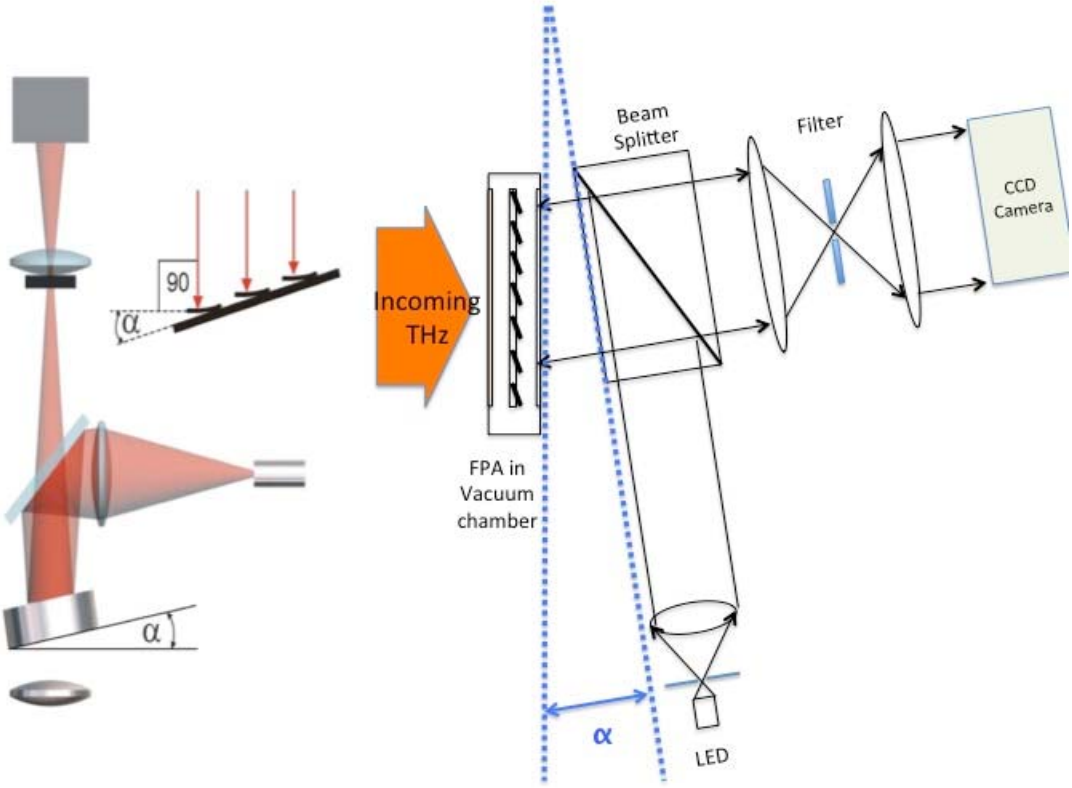

(a) (b)

Figure 14. (a) Illustration of FPA angular adjustment adopted by Grbovic to compensate for intrinsic stress. From [33]. (b) Illustration of FPA angular adjustment adopted.

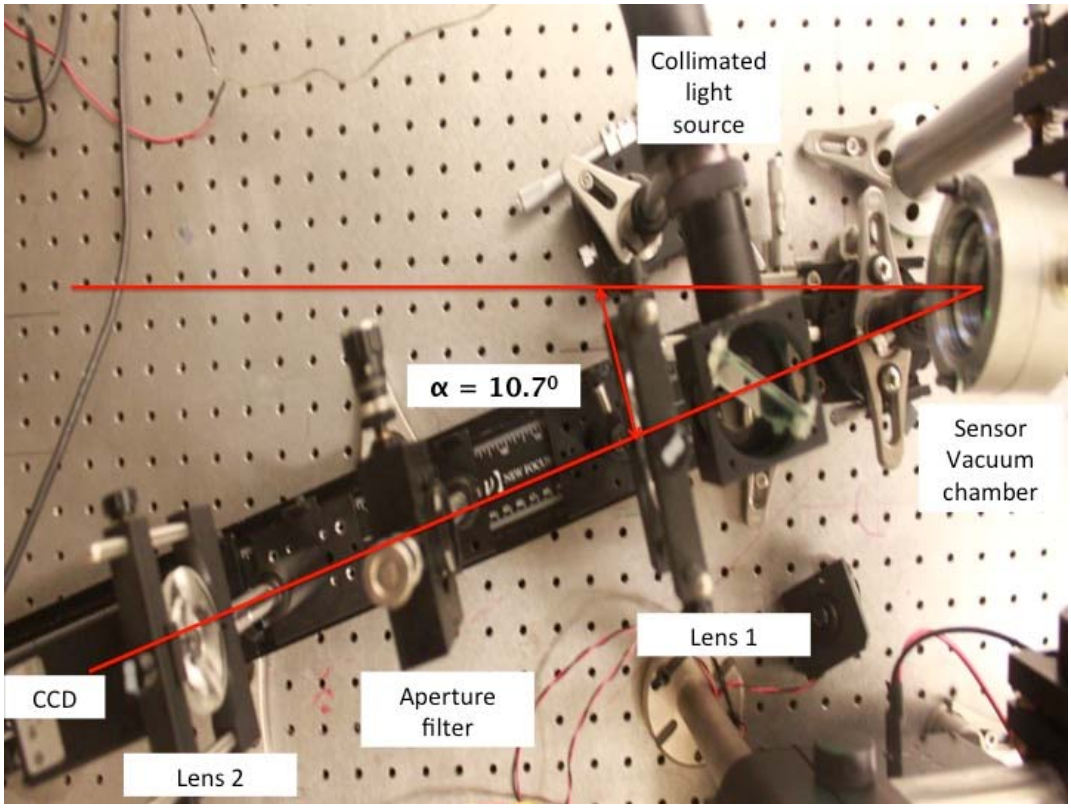

Figure 15. Top view of actual setup of optical system implemented with offsetting optics with the FPA. This is done to ensure maximum THz radiation incident on the sensor and increase sensitivity of the system.

The rationale for the angular offset of the optical system instead of the sensor FPA is as follows:

- To ensure maximum amount of THz radiation incident on the sensor.
- To maximize reflection from the ground planes of the pixels and hence small intensity changes could be detected easily.

As shown in Figure 14, the best image quality is obtained when the offset angle is 10.7^{o}. This value is close to the measured bending of the sensor of about 8^{o}.

B. CONCEPT OF OPERATION OF 4F OPTICAL SYSTEM

The concept of operation of the 4F optical system is illustrated in Figure 16.

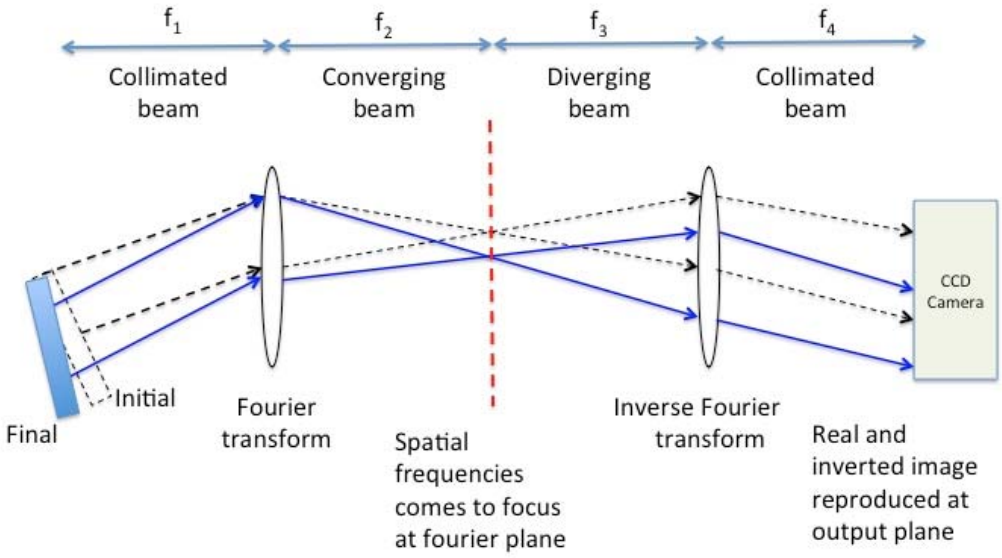

Figure 16. Concept of operation of 4F optical system. The first lens performs Fourier transform of the object and generates the spatial frequencies at the Fourier plane. The second lens performs inverse Fourier transform to reconstruct the original image. Spatial filtering is done at the Fourier plane. Due to deflections of the sensor, reflected rays are focused onto different positions on the Fourier plane. This allows spatial filtering to be performed.

The reflected light from each sensor on the FPA is decomposed into its respective spatial frequencies after passing through the first lens. Essentially, the first lens performs Fourier transform to produce the spatial frequencies of the object to be imaged. This is expressed in Equation (1)

$$F(u,v) = \int_{-\infty}^{\infty} \int_{-\infty}^{\infty} f(x,y) e^{-2\pi i(xu+yv)} dxdy \quad (1)$$

where *F(u,v)* is the image function, *u* and *v* are the two dimensional coordinates in the output plane of the first lens, and *f(x,y)* is the two dimensional coordinates in input plane of the first lens.

Subsequently, the spatial frequencies are focused at the Fourier plane by the first lens and the second lens reproduces the image at the output plane (FPA of the CCD). The second lens basically performs another Fourier transform operation, which essentially is the inverse Fourier transform of the spectrum at the Fourier plane. This produces the original image at the output plane.

By regarding each pixel on the detector as a point source, each pixel when imaged through the optical system is an impulse response. The output signal is then a summation of all the impulse responses of the pixels. Mathematically, it is a convolution of the input signal with an impulse response as in Equation (2):

$$output(x,y) = input(x,y) \otimes h(x,y) \tag{2}$$

where *output(x,y)* is image function at the output plane of the 4F optical system, *input(x,y)* is the object function at the input place, and *h(x,y)* is the impulse response of the optical system. In the proposed design, a 2-axis circular aperture filter with adjustable aperture size is used to allow selective filtering of frequencies. The impulse response of the circular filter is basically an Airy disc and is described in Equation (3) from [40]:

$$h(r) = \frac{J_1(\frac{2\pi Dr}{f\lambda})}{(\frac{2\pi Dr}{f\lambda})} \tag{3}$$

where $r = x^2 + y^2$, J_1 is Bessel function of the first order, D is the diameter of the aperture filter, f is the focal length of the lens used, and λ is the wavelength of the light used.

Based on the convolution theorem, the Fourier transform of a convolution of two functions is just the multiplication of the Fourier transform of the functions in the spatial frequency domain. In Fourier space,

$$OUTPUT(u,v) = INPUT(u,v)H(u,v) \tag{4}$$

where *OUTPUT(u,v)* is the Fourier transform of the output image, *INPUT(u,v)* is the Fourier transform of the image spectrum at the input plane, *H(u,v)* is the Fourier transform of the impulse response, otherwise known as the coherent transfer function. For the Fourier 4F readout system in this thesis, *H(u,v)* can be described as the filtering function of the optical system. In this case, the filtering function changes the value of specific spatial frequencies to be zero.

With the mathematical descriptions in place, it is appropriate to provide the concept of how the Fourier 4F optical system performs spatial filtering. From Figure 18, the concept of the detector image being converted into its respective spatial frequencies at the Fourier plane is shown.

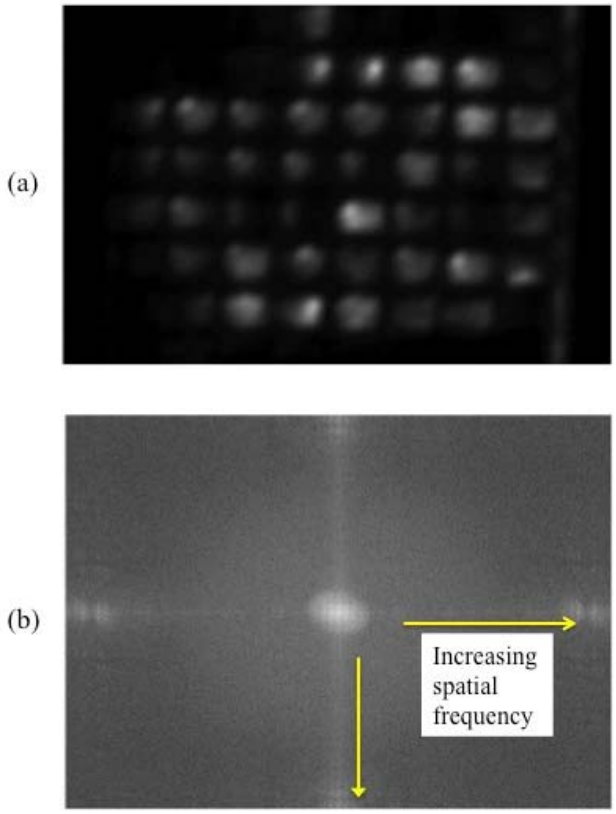

Figure 17. Illustration of an image from the detector decomposed into its respective spatial frequencies. (a) Original image of light reflecting of the pixels from the sensor before passing through the first lens for Fourier transform operations. (b) Fourier transform of the image obtained after passing through the first lens. Highlighted are the relative locations of the spatial frequencies. The Fourier transformation of the image was obtained using MATLAB.

At the Fourier plane, the low spatial frequencies are mainly due to the central part of the sensor, whereby most light is reflected off the absorber ground plane while high spatial frequencies are due to the edges of the absorber. The effect of high-pass and low-pass filtering can be seen from the FPA images in Figure 18. It is apparent that the presence of higher frequencies reveals more details in the image, especially at the edges of each sensor. In addition, a larger aperture also allows more light to reach the CCD. Hence, Figure 18(b) is a brighter image compared to Figure 18(a), even though the amount of illumination remains the same.

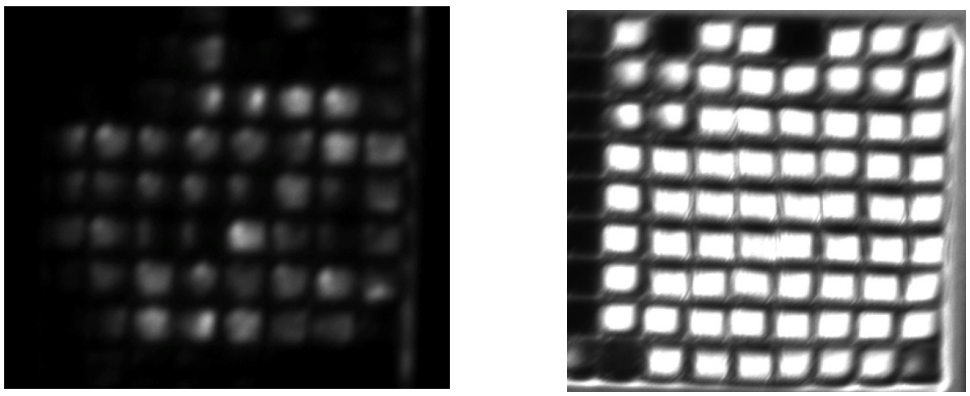

(a) (b)

Figure 18. Reconstructed images of the same original obtained after passing through the Fourier 4F optical readout system with different aperture sizes. (a) Low-pass image obtained with a small aperture opening. (b) Broadband-pass (high + low pass) image obtained with a large aperture opening.

More importantly, for sensitivity in change detection, the aperture diameter must be small enough. Changes in the position of the sensor would cause the light rays from the sensor to be focused at different positions at the Fourier plane. If it hits opaque positions on the filter, it will not be reproduced at the output. Hence, an aperture is used to partially block rays due to deformations in the sensor, which gives the gray scale. Small apertures increase the sensitivity of the optical system at the expense of reducing the amount of light for image reproduction at the CCD camera.

To calculate the theoretical sensitivity of the system, starting from first principles of optics and regarding each pixel as a "pseudo slit," the first minimum is given by

$$\theta = \frac{\lambda}{a} \tag{5}$$

where θ is angle between the normal line of the screen and ray from the pixel to the image on the Fourier plane, λ is the wavelength of the light from the collimated LED assembly, and a is the width of the pixel.

When considering the first lens in the optical system, the angular width of the first minimum on the Fourier plane then becomes

$$\theta = \frac{\lambda f}{a} \tag{6}$$

where f is the focal length of the first lens.

Using Rayleigh's criterion, to be able to resolve the reflected light displacement from the pixel properly, the zero order maximum must shift to the first minimum of the original image. Using Equation (6), with the estimated parameters of λ = 500 nm, f = 10 cm, and a = 200 μm, the optical system is estimated to be sensitive enough able to detect the pixel's angle of deflection of approximately 1.43×10^{-2} deg, which corresponds to a temperature change of 2.86×10^{-3} K on the surface of the sensor.

In summary, the 4F optical system is a preferred optical arrangement for the following reasons.

- Spatial filtering can be performed at the Fourier plane. This makes downstream imaging processing simpler.
- There is no need for focusing optics for the CCD camera as the output rays are collimated.
- The sensitivity of the system can be easily adjusted by varying the diameter of the aperture filter.
-

C. OPTICS ALIGNMENT PROCEDURE

To ensure the proper functioning of the system, various optical components are required to be aligned and configured in the following sequence.

1. ALIGNMENT OF QCL BEAM WITH FOCUSING MIRRORS

As the THz imaging system is operated in transmission mode, it is necessary to produce a broad, collimated THz beam to illuminate the target and produce the THz scene on the MEMS THz sensor. This requires precise alignment of the off axis parabolic (OAP) mirrors.

The alignment of the QCL beam with the focusing OAP mirrors is carried out as follows:

- The f1 (focal length=50.8 mm) OAP mirror is placed at the exit window of the QCL. A semiconductor laser affixed to a beam broadener provides a highly collimated light source. The collimated light source is directed on the f/1 OAP mirror and adjusted in such a way that the focal point of the OAP is formed on the QCL. In addition, to ensure the maximum amount of THz radiation is captured by the f1 OAP mirror, the collimated light needs to illuminate near the center of the OAP.

- Next, the f2 (focal length=101.8 mm) OAP mirror is placed approximately 10 cm away from the f1 mirror. The collimated light source is then directed on the f2 OAP mirror and adjusted such that the focal point of the f2 mirror is near the center of the f1 mirror.

- A microbolometer with Ge lens removed, exposing the microbolometer's sensor FPA, is used to image and confirm the QCL beam pattern produced from the alignment.

2. ALIGNMENT OF 4F OPTICAL SYSTEM

The alignment of the 4F optical system is carried out as follows:

- The 4F optical system is initially placed perpendicular to the MEMS THz sensor. The system is then focused on the substrate plane of the sensor.

- Subsequently, the entire 4F optical system is rotated until the pixels from the sensor appear on the image. Fine adjustments are made and the aperture filter is closed as small as possible.

- The QCL is then turned on and additional adjustments are made to aperture size and position so as to obtain the greatest sensitivity.

D. CCD CAMERA SETTINGS

The camera setup parameters are configured through the camera setup options in the imaging software. The shutter value on the CCD camera is set to a maximum value of 4095. The exposure time is calculated based on the following formula [41]:

$$\text{Exposure Time} = (\text{shutter value setting}) \times 20\ \mu\text{s} \tag{7}$$

Using Equation (7), this translates to an exposure time of 81.9 ms or 12.18 fps. For the setup, the maximum camera exposure time is used to collect more light to form a brighter image for better differential imaging. Moreover, at this setting, the speed of operation of the CCD is still much faster than that compared to the MEMS THz sensor (time constant, $\tau = 0.3$ s) [7]. Thus, the CCD camera operating at the exposure limit is still fast enough for real-time imaging using the MEMS THz sensor.

The camera's sensor has 10-bit dynamic range while the camera output has an 8-bit output range. As the diameter of the aperture used is small (up to approximately 0.5 mm), the amount of light reaching the camera CCD is also correspondingly very low. In order to increase the detectability of light, it is necessary to map a smaller output of the camera's sensor output range to the full dynamic range of the camera output. Thus, a 255 gain value is applied. This corresponds to a 12 dB gain (a 4x amplification) and the output response is shown in Figure 19.

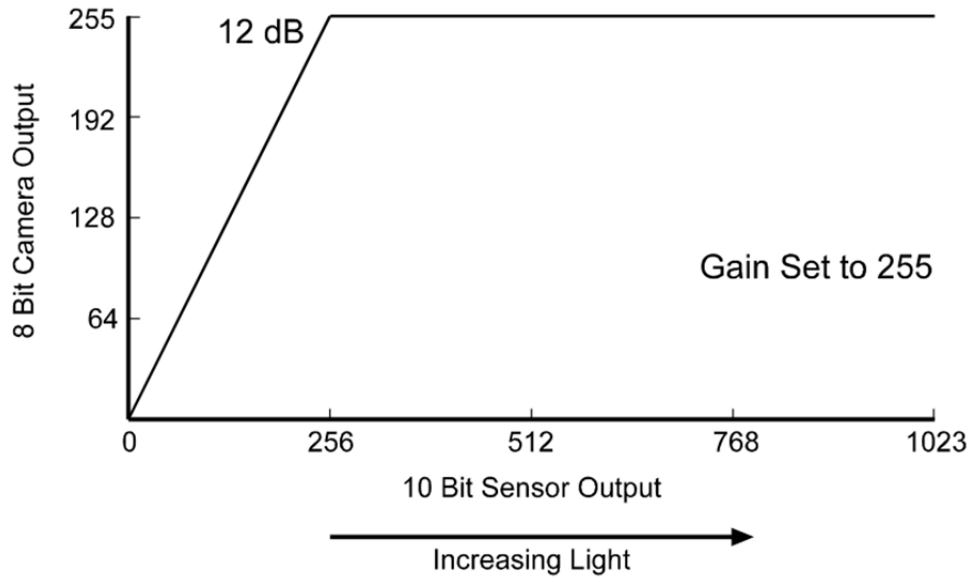

Figure 19. Output due to gain value of 255 being applied. From the graph, it can be observed that the camera output is fully saturated when the sensor's output is only 25 percent. This produces an effective 12 dB gain or 4x magnification. From [42].

THIS PAGE INTENTIONALLY LEFT BLANK

V. RESULTS AND ANALYSIS

This chapter outlines the test procedures and presents the results obtained from the integrated imaging system. An analysis of the results will also be given to draw important conclusions regarding the characteristics and performance of the integrated imaging system. While the intrinsic properties of the MEMS THz sensor have been presented in Chapter III, the focus of the characterization is to assess the performance of the integrated optical readout system.

A. IMAGING RESULTS

Using the integrated optical readout system, imaging is performed while subtracting the background to eliminate the fixed pattern noise. Figure 20(a) shows the image of a QCL beam captured from a commercial microbolometer camera and Figure 20(b) shows the image of the similar QCL beam captured by our integrated optical readout system, which was operated at a PRF of 5 kHz and gated at 500 mHz.

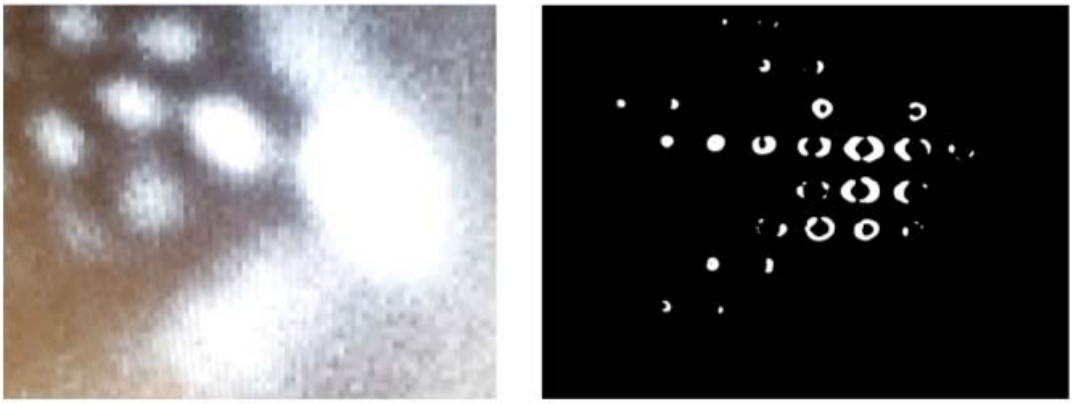

(a) (b)

Figure 20. Imaging of QCL beam. The diffraction pattern is due to far field interference caused by the facets of the QCL laser. The QCL beam is adjusted to give a 'mushroom' shape in order to be imaged on the MEMS THz detector. (a) Image obtained using a commercial IR microbolometer camera. (b) Image obtained using MEMS THz detector with background subtraction. It can be observed that, due to the larger pitch size of the MEMS THz FPA as compared to the microbolometer FPA, it cannot resolve the finer details of the QCL beam.

Due to the larger spacing between the pixels in the MEMS THz sensor, the resolution is much lower than that compared to the QCL beam pattern imaged by the microbolometer camera. An attempt is also made to image objects under THz illumination. As THz radiation cannot penetrate through metal, a thin metal rod is placed between the OAP mirrors to act as a target (see Figure 21). The metal rod (diameter ~ 2 mm) is then moved about to be imaged on the detector and incite a response. The gating of the QCL is switched off for the QCL to operate in continuous mode to see the movement of the metal rod more easily. Figure 21 shows the results of the imaging for the moving metal rod.

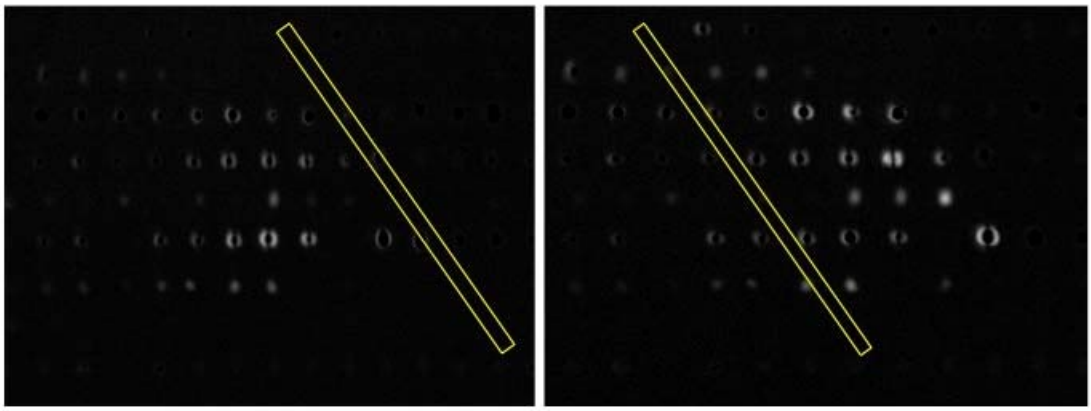

Figure 21. A thin metal rod moving about and imaged under THz illumination using the integrated optical readout system. The position of the metal rod is highlighted in yellow, as the resolution of the system is not able to provide a clearer outline of the metal rod. As the metal rod moves about the illumination scene, the pixels in the detector start to flicker. The 'flickering' effect is due to the metal rod blocking THz radiation. This effect is more apparent in the video recording of the frames captured above.

From Figure 21, it can be observed that the effects of the large pitch of the sensor limit the resolution of the integrated optical readout system. The system is unable to resolve the outline of the metal rod. However, as the metal rod moves through the illumination scene, it blocks THz radiation and causes the sensors to deflect. This makes the THz seem to 'flicker.' Hence, while the optical readout system suffers from poor

resolution, it is sensitive enough to detect small changes in THz radiation due to a small moving metallic object.

B. SYSTEM THERMAL RESPONSE CHARACTERIZATION

The thermo-mechanical sensitivity ($dT/d\theta$=0.2 Deg K^{-1}) of the MEMS THz sensor was presented in earlier chapters. It is an indication of the thermal sensitivity of the pixel itself and does not fully describe the thermal sensitivity of the integrated readout system. It was expected that the integrated thermal responsivity of the entire system, if integrated and implemented well, would approximate to the value obtained for the thermo-mechanical sensitivity of the MEMS THz sensor. However, instead of monitoring the angle of deformation of the sensor as the temperature varies, the change in the grey pixel value is used instead. The thermal response characterization aims to measure the change in grey level values per degree change in temperature of the sensor. The value obtained is the combined thermal sensitivity of the MEMS THz sensor and the 4F optical readout system. To obtain the thermal response of the system, the setup is configured as shown in Figure 22.

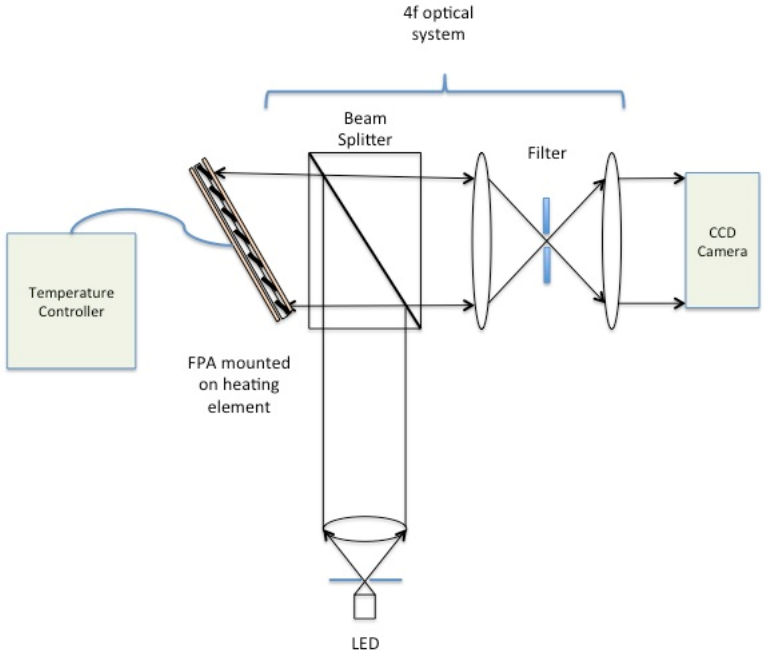

Figure 22. Imaging setup for thermal response characterization. 4F optical system is used to detect changes in the sensor deflection as temperature changes.

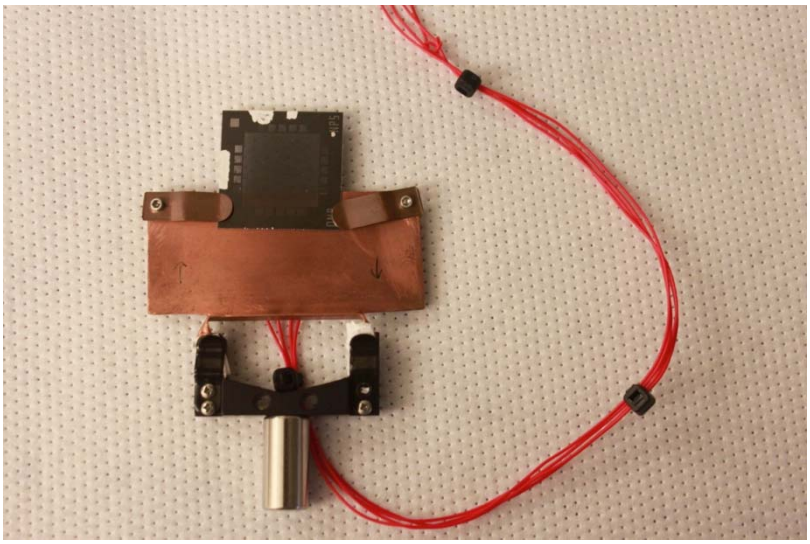

Figure 23. MEMS detector mounted on copper heating element to monitor thermal response of sensor in 4F optical system.

The temperature of the sensor can be varied by mounting it onto a copper heating plate (see Figure 23). The copper heating plate would change the temperature of the sensor in a precise and incremental manner for the integrated thermal readout characterization. The temperature is swept from 297 K to 303 K (24^{o} C to 30^{o} C) with 0.1 K increments using a Thorlabs TC200 temperature controller. The light beam reflected off by the pixels over the CCD camera would deflect and be correspondingly filtered by the 4F imaging system as the temperature increases.

The change in intensity of the reflected light is monitored by the image processing software using background subtraction as described in earlier sections. An area on the sensor, corresponding to 3 x 3 pixels is selected to measure their average gray values as temperature changes. To ensure that the maximum thermal response is extracted from the test, the sensor FPA is also rotated on a rotating platform mount to compensate for the intrinsic bending of the sensor. The 3 x 3 pixels, which are selected to be tested, are based on initial test runs that showed they were totally dark at 24^{o} C and reflecting maximum amount of light at 30^{o} C. These pixels also need to be next to each other in the array. Each pixel's gray level response is individually measured and the permanently dark areas of the substrate are not considered. The average values of the gray levels are then computed.

The average gray values from the 3 x 3 pixel area as a function of temperature change are shown in the graph in Figure 24.

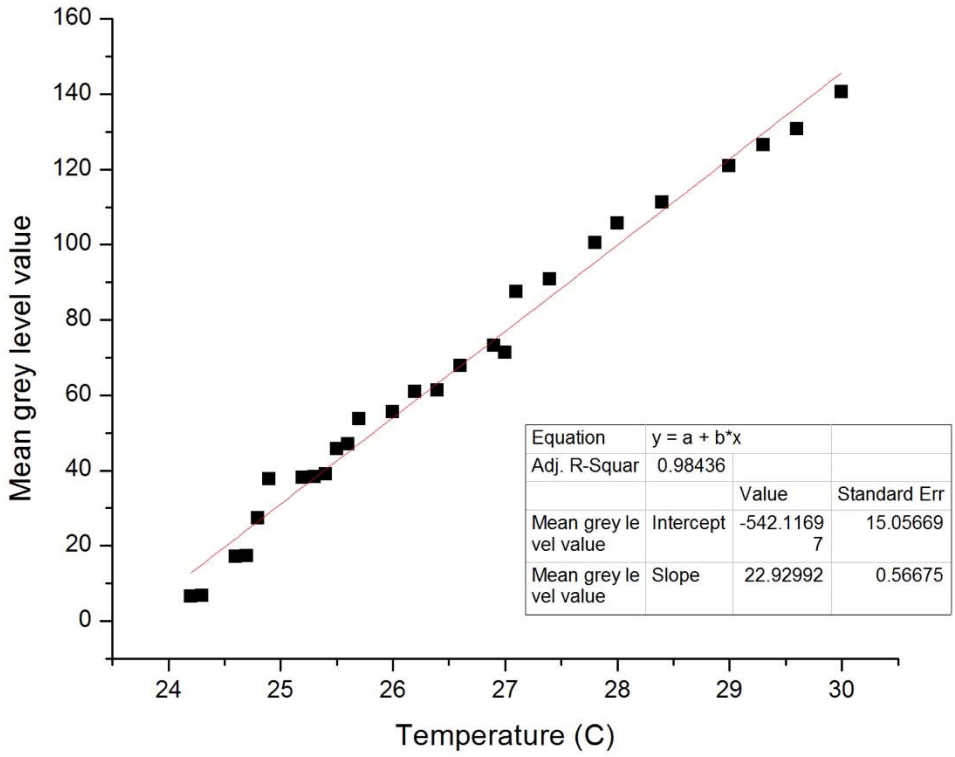

Figure 24. Plot of average gray level as a function of temperature of the sensor array.

From the data, it can be observed that the thermal response of the integrated system for the operating temperature range of 297 K to 303 K (24^{o}C to 30^{o}C) is approximately 23 gray levels per Kelvin.

C. EFFECT OF APERTURE SIZE

The effect of the aperture size becomes apparent when imaging is performed using the integrated optical readout system. Using the same setup used for the system thermal response characterization, the background subtracted images for different aperture sizes are obtained for the same temperature range.

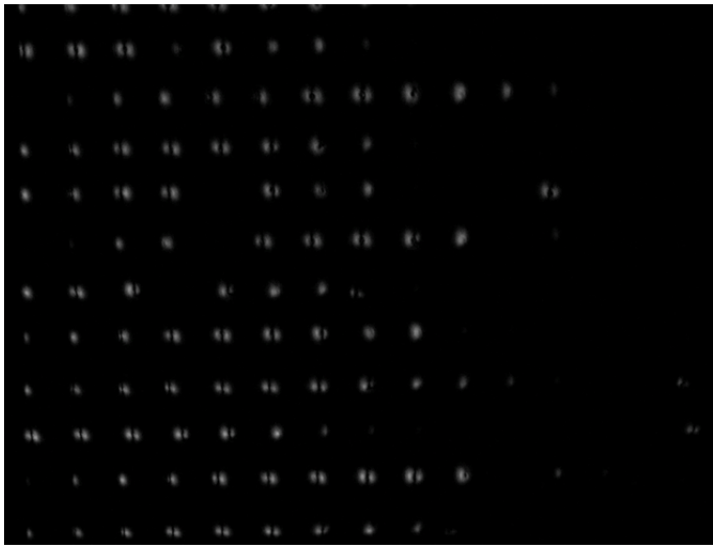

(a)

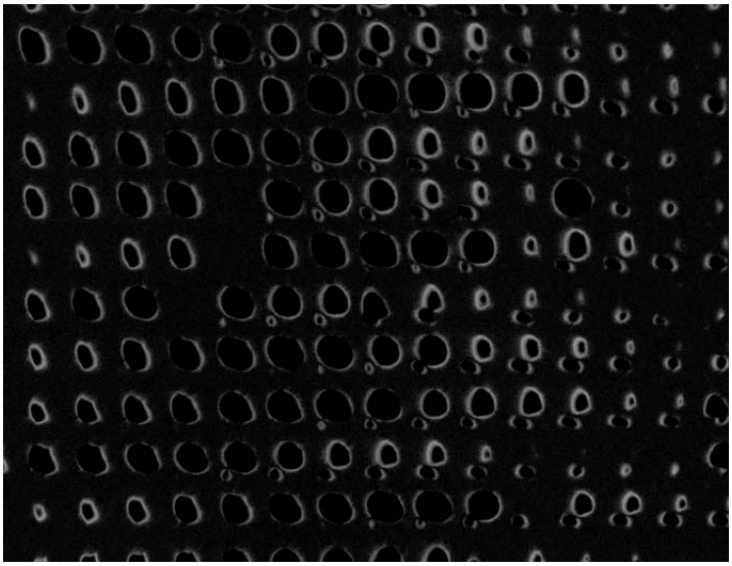

(b)

Figure 25. Background subtracted images for aperture size (a) 0.5 mm (b) 5 mm.

From Figure 26, it can be observed that aperture size dramatically changes the nature of the image produced by the optical readout system. It can be observed that the smaller aperture size results in the better filtering of lower spatial frequencies in the diffraction pattern in the Fourier plane. A larger aperture size results in the appearance of the higher spatial frequencies of the diffraction patterns. While the lower spatial frequencies are displaced as well, they are not filtered, and hence they do not show up in the background-subtracted image. This is evident in Figure 25(b) where the dark rings, which are the lower spatial frequencies, and the faint glow surround the dark rings are the higher spatial frequencies of the diffraction pattern.

THIS PAGE INTENTIONALLY LEFT BLANK

VI. CONCLUSIONS

In this thesis, an optical readout scheme was successfully developed based on the Fourier 4F optical system. The optical readout system was also successfully integrated with the MEMS THz detector. A QCL provided the THz illumination while post image processing performed background subtraction to obtain the THz scene on the detector.

The concept of using optical readout to probe the detector was validated, as the integrated system was able to reproduce image of the QCL beam pattern due to the relative deflection of a large number of pixels. This was an important step in developing an image acquisition system based on optical readout. In addition, the physics of the Fourier 4F system was studied and image outputs due to spatial filtering were checked and compared with established theories. This is to provide confidence in the ability of the Fourier 4F optical readout system to be able to enhance the sensitivity of the readout system. The sensitivity of the system is based on reflected light being blocked by the aperture as the sensor is deflected as well as optical spatial filtering.

Through these studies, it was noted that there is room for the optical readout system to be further optimized for future work. For better collimation and lesser loss of THz radiation energy, a custom OAP mirror can be mounted on the QCL copper head to collimate and focus the THz laser before exiting the cryostat assembly. (This requirement was noted during the assembly of the optical system. However, the OAP was still in the process of fabrication and not available for testing.) This allows more energy to reach the MEMS THz detector to excite a greater number of pixels for better image reconstruction.

In addition, the components used in the Fourier 4F optical system can be improved. The tested setup had the components aligned on an optical rail, which had considerable light leakage. Moving forward, lens tube systems can be designed around the Fourier 4F optical system concept to enhance the overall system. It is envisaged that lens tube systems can reduce distortions and aberrations as well as make the overall system more compact.

THIS PAGE INTENTIONALLY LEFT BLANK

LIST OF REFERENCES

[1] J. E. Bjarnason, T. L. J. Chan, A. W. M. Lee, M. A. Celis, and E. R. Brown, "Millimeter-wave, terahertz, and mid-infrared transmission through common clothing," *Appl. Phys. Lett.,* vol. 85, pp. 519–521, 2004.

[2] J. F. Federici, B. Schulkin, F. Huang, D. Gary, R. Barat, F. Oliveira, and D. Zimdars, "THz imaging and sensing for security applications: Explosives, weapons and drugs," *Semiconductor Science and Technology,* vol. 20, p. S266, 2005.

[3] J. F. Federici, D. Gary, R. Barat, and D. Zimdars, "THz standoff detection and imaging of explosives and weapons," in *Proc. SPIE,* vol. 5781, 2005, pp. 75–84.

[4] A. Y. Pawar, D. D. Sonawane, K. B. Erande, and D. V. Derle, "Terahertz technology and its applications," *Drug Invention Today,* vol. 5, pp. 157–163, 6, 2013.

[5] B. N. Behnken, G. Karunasiri, D. R. Chamberlin, P. R. Robrish, and J. Faist, "Real-time imaging using a 2.8 THz quantum cascade laser and uncooled infrared microbolometer camera," *Opt. Lett.,* vol. 33, pp. 440–442, Mar. 2008.

[6] M. Lowe, "Imaging of 3.4 THz quantum cascade laser beam using uncooled microbolometer camera," M.S. thesis, Naval Postgraduate School, Monterey, CA, 2006.

[7] F. Alves, D. Grbovic, B. Kearney, and G. Karunasiri, "Microelectromechanical systems bimaterial terahertz sensor with integrated metamaterial absorber," *Opt. Lett.,* vol. 37, pp. 1886–1888, Jun. 2012.

[8] F. Alves, B. Kearney, D. Grbovic, N. V. Lavrik, and G. Karunasiri, "Strong terahertz absorption using SiO2/Al based metamaterial structures," *Appl. Phys. Lett.,* vol. 100, 2012.

[9] F. Alves, D. Grbovic, B. Kearney, and G. Karunasiri, "High sensitivity metamaterial based bi-material terahertz sensor," in *Proc. SPIE,* vol. 8624, 2013, pp. 862411–862419.

[10] F. Alves, D. Grbovic, and G. Karunasiri, "Investigation of MEMS bi-material sensors with metamaterial absorbers for THz imaging," in *Proc. SPIE,* vol. 9083, 2014, pp. 90830-90830-9.

[11] P. G. Datskos, S. Rajic, L. R. Senesac, D. D. Earl, B. M. Evans III, J. L. Corbeil, and I. Datskou, "Optical readout of uncooled thermal detectors," in *Proc. SPIE,* vol. 4130, 2000, pp. 185–197.

[12] M. Erdtmann, L. Zhang, G. Jin, S. Radhakrishnan, G. Simelgor, and J. Salerno, "Optical readout photomechanical imager: from design to implementation," in *Proc. SPIE,* vol. 7298, 2009, pp. 72980-72980-8.

[13] P. R. Norton, M. Mao, T. M. Perazzo, Y. Zhao, O. Kwon, A. Majumdar, and J. B. Varesi, "Micro-optomechanical infrared receiver with optical readout: MIRROR," in *Proc. SPIE,* vol. 4028, 2000, pp. 72–78.

[14] E. Montagner, "Optical readout system for bi-material terahertz sensors," M.S. thesis, Naval Postgraduate School, Monterey, CA, 2011.

[15] C. O'Sullivan J. and A. Murphy, *Terahertz Sources, Detectors, and Optics*. Bellingham, WA, 2012.

[16] E. Alekseev and D. Pavlidis, "GaN gunn diodes for THz signal generation," in *2000 IEEE MTT-S Int. Microw. Symp. Dig.,* vol. 3, 2000, pp. 1905–1908.

[17] T. O. Klaassen, J. Niels Hovenier, R. K. Zhukavin, D. M. Gaponova, A. Muravjov, E. E. Orlova, V. N. Shastin, S. G. Pavlov, H. Hubers, H. Riemann, and A. G. van der Meer, "The emission spectra of optically pumped si-based THz lasers," in *Proc. IEEE Tenth Int. Conf. Terahertz Electron.,* 2002, pp. 89–92.

[18] A. Ali Rostami, H. Rasooli and H. Baghban, "Terahertz technology fundamentals and applications," *Lecture Notes in Electrical Engineering,* vol. 77, pp. vii, 2011.

[19] M. Glyavin, A. Luchinin, V. Manuilov, M. Moiseev, A. Sedov, and V. Zapevalov, "Development of powerful terahertz gyrotrons," in *2010 International Kharkov Symposium on Physics and Engineering of Microwaves, Millimeter and Submillimeter Waves (MSMW)*, 2010, pp. 1–6.

[20] J. Shikata, M. Sato, T. Taniuchi, H. Ito, and K. Kawase, "Enhancement of terahertz-wave output from LiNbO3 optical parametric oscillators by cryogenic cooling," *Opt. Lett.,* vol. 24, pp. 202–204, Feb. 1999.

[21] S. Preu, S. Malzer, L. J. Wang, and A. C. Gossard, "Tunable, continuous-wave Terahertz photomixer sources and applications," *J. Appl. Phys.,* vol. 109, 2011.

[22] F. Castellano, H. Beere, D. Ritchie, and M. S. Vitiello, "Polymeric waveguide components for THz quantum cascade laser outcoupling," in *Proc. SPIE,* vol. 8985, 2014, pp. 89851F-89851F-6.

[23] Y. Lee, Ed., *Principles of Terahertz Science and Technology.* Oregon: Springer, 2009.

[24] M. J. Coppinger, N. A. Sustersic, J. Kolodzey, and T. H. Allik, "Sensitivity of a vanadium oxide uncooled microbolometer array for terahertz imaging," *Optical Engineering,* vol. 50, pp. 053206-053206-5, 2011.

[25] C. O'Sullivan and A. Murphy, "Pyroelectric detectors," in *Field Guide to Terahertz Sources, Detectors, and Optics*, J. Greivenkamp, Ed. Washington: SPIE, 2012, p. 49.

[26] E. Ledwosinska, A. Guermoune, M. Siaj, and T. Szkopek, "Fabrication and characterization of suspended graphene membranes for miniature Golay cells," in *Proc. SPIE,* vol. 8624, 2013, pp. 86240U-86240U-8.

[27] H. Luo, H. C. Liu, C. Y. Song, Z. R. Wasilewski, A. J. SpringThorpe, and J. C. Cao, "Terahertz quantum well photodetectors," in *Proc.SPIE,* vol. 6308, 2006, pp. 63080N-63080N-6.

[28] T. Suzuki, T. Yasui, H. Fujishima, T. Nozokido, M. Araki, O. Boric-Lubecke, V. M. Lubecke, H. Warashina, and Koji Mizuno, "Reduced low-frequency noise Schottky barrier diodes for terahertz applications," *IEEE Trans. Microw. Theory Tech.,* vol. 47, pp. 1649–1655, 1999.

[29] T. Yasui, A. Nishimura, T. Suzuki, K. Nakayama, and S. Okajima, "Detection system operating at up to 7 THz using quasioptics and Schottky barrier diodes," *Rev. Sci. Instrum.,* vol. 77, pp. 066102–3, 2006.

[30] D. T. Petkie, C. Casto, F. C. D. Lucia, S. R. Murrill, B. Redman, R. L. Espinola, C. C. Franck, E. L. Jacobs, S. T. Griffin, C. E. Halford, J. Reynolds, S. O'Brien, and D. Tofsted, "Active and passive imaging in the THz spectral region: phenomenology, dynamic range, modes, and illumination," *Opt. Soc. Am. B.,* vol. 25, pp. 1523–1531, Sep. 2008.

[31] C. D. W. Jones, C. A. Bolle, R. Ryf, M. E. Simon, F. Pardo, V. A. Aksyuk, W. Y. Lai, J. E. Bower, J. F. Miner, F. P. Klemens, R. A. Cirelli, T. W. Sorsch, E. J. Ferry, L. A. Fetter, C. Pai, J. A. Taylor, B. Vyas, G. P. Watson, B. Stekas, M. R. Baker, A. R. Papazian, N. R. Basavanhally, W. M. Mansfield, A. Kornblit, R. C. Keller, J. V. Gates, and A. P. Ramirez, "MEMS thermal imager with optical readout," *Sensors and Actuators A: Physical,* vol. 155, p. 47, 2009.

[32] F. Alves, D. Grbovic, B. Kearney, N. V. Lavrik, and G. Karunasiri, "Bi-material terahertz sensors using metamaterial structures," *Opt. Express,* vol. 21, pp. 13256–13271, Jun. 2013.

[33] G. Dragoslav, "Imaging by detection of infrared photons using arrays of uncooled micromechanical detectors," Ph.D. dissertation, Univ. of TN, Knoxville, pp. 26–30, 2008.

[34] Microtech Instruments. (2003). Transmission spectra of tsurupica and polyethylene, *MT Instruments Datasheet* [Online]. Available: http://www.mtinstruments.com/downloads/THz%20Lenses%20and%20Windows%20Datasheet.pdf.

[35] M. Tonouchi, “Cutting-edge terahertz technology,” *Nat. Photon,* vol. 1, pp. 97–105, 2007.

[36] M. W. R. Ng, “High power quantum cascade laser for terahertz imaging,” M.S. thesis*,* Naval Postgraduate School, Monterey, CA, 2012.

[37] E. J. Botcherby, R. Juškaitis, M. J. Booth, and T. Wilson, “An optical technique for remote focusing in microscopy,” *Opt. Commun.,* vol. 281, pp. 880–887, Feb. 2008.

[38] R. Jain, R. Kasturi, and B. G. Schunck, “Image filtering,” in *Machine Vision*. New York: McGraw-Hill, 1995, p. 112.

[39] Mouser Electronics. (2004). 941-XPEGRNL100A01 technical specifications. [Online]. Available: http://www.mouser.com/ProductDetail/Cree-Inc/XPEGRN-L1-0000-00A01/?qs=y%252bJdrdj3vZrKJy3Axu5%252blw==.

[40] A. Ghatak, “Fraunhofer diffraction,” in *OPTICS*, 2nd ed., New York: McGraw-Hill, 2005.

[41] Basler. (2011). Basler A630f - User’s manual. [Online]. Available: http://www.baslerweb.com/linklist/1/6/0/4/6/DA00074303_A630f_Users_Manual.pdf.

[42] Basler. (2011). Configuring the A600x camera. [Online]. Available: http://www.baslerweb.com/media/documents/DA00056109%20A600f%20Users%20Manual.pdf.

INITIAL DISTRIBUTION LIST

1. Defense Technical Information Center
   Ft. Belvoir, Virginia

2. Dudley Knox Library
   Naval Postgraduate School
   Monterey, California